Title

Paradoxical effects of obesity on T cell function during tumor progression and PD-1 checkpoint blockade

Journal

Nature Medicine, 25(1)

ISSN

1078-8956

Authors

Wang, Ziming

Aguilar, Ethan G

Luna, Jesus I

et al.

Publication Date

2019

DOI

10.1038/s41591-018-0221-5

Peer reviewed

DispatchDate: 04.10.2018 · ProofNo: 221, p.1

nature medicine

ARTICLES

https://doi.org/10.1038/s41591-018-0221-5

Paradoxical effects of obesity on T cell function during tumor progression and PD-1 checkpoint blockade

Ziming Wang[1,20], Ethan G. Aguilar[1,20], Jesus I. Luna[1], Cordelia Dunai[1], Lam T. Khuat[1], Catherine T. Le[1], Annie Mirsoian[1], Christine M. Minnar[1], Kevin M. Stoffel[1], Ian R. Sturgill[1], Steven K. Grossenbacher[1], Sita S. Withers[2], Robert B. Rebhun[2], Dennis J. Hartigan-O'Connor[3,4,5], Gema Méndez-Lagares[4,5], Alice F. Tarantal[5,6,7], R. Rivkah Isseroff[1,8], Thomas S. Griffith[9], Kurt A. Schalper[10], Alexander Merleev[1,11], Asim Saha[12], Emanual Maverakis[1,11], Karen Kelly[13], Raid Aljumaily[14], Sami Ibrahimi[14], Sarbajit Mukherjee[14], Michael Machiorlatti[15], Sara K. Vesely[15], Dan L. Longo[16], Bruce R. Blazar[17], Robert J. Canter[18], William J. Murphy[1,13,21]* and Arta M. Monjazeb[19,21]

The recent successes of immunotherapy have shifted the paradigm in cancer treatment, but because only a percentage of patients are responsive to immunotherapy, it is imperative to identify factors impacting outcome. Obesity is reaching pandemic proportions and is a major risk factor for certain malignancies, but the impact of obesity on immune responses, in general and in cancer immunotherapy, is poorly understood. Here, we demonstrate, across multiple species and tumor models, that obesity results in increased immune aging, tumor progression and PD-1-mediated T cell dysfunction which is driven, at least in part, by leptin. However, obesity is also associated with increased efficacy of PD-1/PD-L1 blockade in both tumor-bearing mice and clinical cancer patients. These findings advance our understanding of obesity-induced immune dysfunction and its consequences in cancer and highlight obesity as a biomarker for some cancer immunotherapies. These data indicate a paradoxical impact of obesity on cancer. There is heightened immune dysfunction and tumor progression but also greater anti-tumor efficacy and survival after checkpoint blockade which directly targets some of the pathways activated in obesity.

Recent advances in our understanding of the mechanisms of immune regulation have led to major clinical breakthroughs in cancer, including the use of inhibitors of the PD-1/PD-L1 (PD-(L)1) axis, or 'checkpoint blockade'[1–3]. PD-(L)1 signaling is central to both initial T cell priming and later T cell exhaustion, which occurs with aging or chronic antigen stimulation resulting in impairment of proliferative and functional abilities[4]. Blockade of this pathway markedly augments T cell responses in a variety of viral and cancer models[5–8]. However, despite the success of PD-(L)1 blockade in multiple malignancies including melanoma and lung, renal, and bladder cancer, these therapies fail to generate sustained benefits in most patients. Extensive efforts are underway to elucidate biomarkers and mechanisms of response[9]. Many studies have focused on the tumor microenvironment (TME) as well as mutational or antigenic load, but patient-associated factors such as sex, age, body mass index (BMI) and immunological history (for example, pathogen exposure) are also likely to profoundly impact immune responses and yet are poorly understood.

Obesity, defined by increased BMI (≥30 kg/m^2), reflecting visceral fat accumulation[10], is reaching pandemic proportions. Obesity has been associated with numerous comorbidities such as diabetes, heart disease and cancer[10–12] and represents a significant societal burden accounting for >20% of the total annual U.S. healthcare expenditure[13]. Although obesity is characterized by a 'meta-inflammatory'

[1]Department of Dermatology, UC Davis School of Medicine, Sacramento, CA, USA. [2]Department of Surgical and Radiological Sciences, School of Veterinary Medicine, UC Davis, Davis, CA, USA. [3]Division of Experimental Medicine, UC San Francisco, San Francisco, CA, USA. [4]Department of Medical Microbiology and Immunology, UC Davis, Davis, CA, USA. [5]California National Primate Research Center, UC Davis, Davis, CA, USA. [6]Department of Pediatrics, UC Davis School of Medicine, Davis, CA, USA. [7]Department of Cell Biology and Human Anatomy, UC Davis, Davis, CA, USA. [8]Dermatology Service, Sacramento VA Medical Center, Mather, CA, USA. [9]Department of Urology, Center for Immunology, Masonic Cancer Center, Microbiology, Immunology, and Cancer Biology Graduate Program, University of Minnesota, Minneapolis, MN, USA. [10]Department of Pathology & Translational Immunooncology Laboratory, Yale University School of Medicine, New Haven, CT, USA. [11]Immune Monitoring Core, UC Davis Comprehensive Cancer Center, Sacramento, CA, USA. [12]Masonic Cancer Center and Department of Pediatrics, University of Minnesota, Minneapolis, MN, USA. [13]Department of Internal Medicine, Division of Hematology and Oncology, UC Davis School of Medicine, Sacramento, CA, USA. [14]Department of Internal Medicine, Section of Hematology and Oncology, University of Oklahoma Health Sciences Center, Oklahoma City, OK, USA. [15]Department of Biostatistics and Epidemiology, University of Oklahoma Health Sciences Center, Oklahoma City, OK, USA. [16]Laboratory of Genetics and Genomics, National Institute on Aging, NIH, Baltimore, MD, USA. [17]Masonic Cancer Center and Division of Blood and Marrow Transplantation, Department of Pediatrics, University of Minnesota, Minneapolis, MN, USA. [18]Division of Surgical Oncology, Department of Surgery, UC Davis Comprehensive Cancer Center, UC Davis School of Medicine, Sacramento, CA, USA. [19]Department of Radiation Oncology, UC Davis Comprehensive Cancer Center, UC School of Medicine, Sacramento, CA, USA. [20]These authors contributed equally: Ziming Wang, Ethan G. Aguilar. [21]These authors jointly supervised: William J. Murphy, Arta M. Monjazeb. *e-mail: wmjmurphy@ucdavis.edu

state with dysregulated immune responses and 'inflammaging'[12], little is understood about the impact of obesity on immune responses during cancer progression and immunotherapy. This is confounded by the use, in most preclinical cancer models, of young lean mice that fail to recapitulate the clinical scenario of the elderly cancer patient. Surprisingly, recent clinical analyses demonstrate that obesity is associated with improved response and survival of cancer patients treated with targeted therapy and checkpoint blockade immunotherapy, although a mechanistic link was not elucidated[14,15]. In this study, we investigated the impact of obesity on T cell responses and demonstrate a significant impact of obesity on the PD-(L)1 axis, immune aging and dysfunction across multiple species and cancer models. In particular, we demonstrate a marked effect of obesity on tumor progression in mice as well as on clinical outcomes in cancer patients treated with PD-(L)1 checkpoint blockade stratified by body mass. These studies highlight the contrasting and paradoxical effects, both positive and negative, of obesity on cancer immune responses in the context of immunotherapy.

Results

Obesity-related T cell dysfunction across multiple species. We investigated T cell phenotype and function in control-diet mice (control, 10% fat diet) versus diet-induced obese mice (DIO, 60% fat diet) at 6 months (Supplementary Fig. 1a–g) and 11–12 months of age (Fig. 1a–f and Supplementary Figs. 2, 3). DIO mice had a marked increase in subcutaneous and visceral adipose tissue, as demonstrated by magnetic resonance imaging (Supplementary Fig. 3a,b). Non-fasting glucose and hemoglobin A1c levels were within normal limits in both DIO and control mice (Supplementary Figs. 1b,c, 2a). At 6 months of age, DIO mice had an increased frequency of PD-1+ T cells in the liver (Supplementary Fig. 1f,g). By 11–12 months of age, DIO mice exhibited a significant increase in dysfunctional exhausted T cells in peripheral blood, liver, and spleen. Specifically, DIO mice had an increase in the frequency of memory T cells in the peripheral blood (Supplementary Fig. 2b) and liver (Fig. 1b). Further analysis showed a >2-fold increase in PD-1 expression in DIO versus control T cells (Fig. 1c and Supplementary Fig. 2c). Similar results were seen when examining CD4+ and CD8+ T cell subsets in 6 and 11- to 12-month-old mice (Supplementary Figs. 1f,g, 2d,e). To determine whether increased PD-1 expression in DIO mice was indicative of T cell dysfunction, we examined hallmarks of exhaustion, including diminished proliferative function and cytokine production. Ex vivo stimulated polyclonal T cells from DIO mice demonstrated reduced proliferative capacity, as well as reduced IFNγ and TNFα production compared with control (Fig. 1d,f), and, again, similar results were seen when examining CD4+ and CD8+ T cell subsets (Supplementary Fig. 3). We next assessed the impact of obesity in outbred non-human primates (NHP, rhesus macaques) and humans and observed a remarkably similar pattern. T cells from spontaneously obese NHPs demonstrated a significant increase in the memory pool and PD-1 expression, while also showing reduced proliferative capacity compared with non-obese NHP (Fig. 1g,h and Supplementary Fig. 4a–f). Healthy human volunteers were categorized into obese (BMI≥30) and non-obese (BMI<30) cohorts (Supplementary Fig. 4g and Supplementary Table 1). T cells from these obese donors also demonstrated a significant increase in PD-1 expression and decreased proliferative function compared with non-obese donors (Fig. 1i,j). Thus, across multiple species, we observed increased T cell exhaustion and dysfunction in obese subjects, providing novel data to support an obesity associated phenotype of immune dysfunction.

Obesity promotes tumor growth and T cell exhaustion. We next studied the consequences of obesity on tumor immunity. A confounding issue in preclinical cancer modeling is the direct impact that obesity has on tumor growth kinetics[16], which may obscure the effects of obesity on the immune response to the tumor. B16 melanoma tumors grew significantly faster in 6-month old DIO mice compared with control counterparts (Fig. 2a and Supplementary Fig. 5a). Tumors in DIO mice exhibited increased metabolic activity as demonstrated by increased ^{18}F-fluorodeoxyglucose (FDG) uptake on positron emission tomography (PET)/computed tomography (CT) scans (Fig. 2b and Supplementary Fig.5b). We observed greater ulceration, necrosis, and invasion into subcutaneous fat by melanoma tumors in DIO mice (Supplementary Fig. 5c). Consistent with our previous findings in non-tumor bearing mice, T cells in the TME of DIO mice demonstrated features of exhaustion. Specifically, DIO mice had a significantly higher frequency of tumor-infiltrating CD8+ T cells (CD8+ TILs) expressing PD-1, Tim3 and Lag3 and lower proliferation by Ki67 compared to control mice as assessed by flow cytometry (Fig. 2c–f and Supplementary Fig. 5d). Because regulatory T-cells (T_{regs}) play a role in the TME and have been noted to be altered in obesity[17], we also examined T_{regs} in the TME. We did not observe differences in the frequency of T_{regs} between DIO and control mice (Supplementary Fig. 5e), nor was there a difference in PD-L1 expression in the TME (Supplementary Fig. 5f). Interestingly, *Cpt1a* gene expression, a master regulator of fatty acid oxidation, was upregulated in both tumors and CD8+ T cells of DIO mice (Supplementary Fig. 5g). *Cpt1a* was recently identified as being upregulated in early-stage exhausted T cells after lymphocytic choriomeningitis virus infection and has been suggested as a potential driver of the metabolic changes leading to exhaustion[18]. We observed similar results with 4T1 breast carcinoma cells in DIO BALB/c mice in terms of tumor growth (Supplementary Fig. 5h–j) and TIL PD-1 expression (Fig. 2g) demonstrating these phenomena across strains and tumor types.

In addition to differences in the TME, the frequency of PD-1+ T cells was significantly increased systemically in the liver, spleen, and draining lymph nodes of tumor bearing DIO mice (Supplementary Fig. 6). This finding is in contrast to non-tumor-bearing 6-month-old DIO mice, in which differences were observed only in the liver (Supplementary Fig. 1), indicating that tumor challenge accelerated the exhaustion phenotype in 6-month-old DIO mice inducing an exhausted systemic phenotype resembling 11- to 12-month-old DIO mice. This coincided with a higher expression of transcription factor Eomes and a lower expression of T-bet on PD-1+CD8+ T cells in liver, spleen, and draining lymph nodes of 6-month-old tumor-bearing DIO mice compared to age-matched tumor-bearing controls (Supplementary Fig. 6c,e,g,h). Elevated expression of Eomes and decreased levels of T-bet are well-known markers of T cell exhaustion[19–21]. We observed the frequency of PD-1+ T cells in the visceral fat to be generally higher than that in other organs (Supplementary Fig. 6i-j), which is in agreement with recent reports[22].

We next defined the molecular differences between sorted (>95% purity) CD8+ memory T cells from the spleens and lymph nodes of B16-bearing control and DIO mice using transcriptomic analysis. Categorical clustering adjusted from previously described canonical T cell exhaustion and effector markers[23] corroborated the results of our tumor T cell-phenotyping, demonstrating upregulation of exhaustion-related transcripts and downregulation of effector-related transcripts in T cells from DIO mice (Fig. 2h). Differential profile analysis also demonstrated marked global transcriptional differences of CD8+ T cells from control versus DIO mice (Supplementary Fig. 7a). This functional categorical clustering of markers was generated based on previously published data[24]. T cells from tumor-bearing DIO mice upregulated anergy-, senescence-, and TGF-β-associated genes as well as genes previously associated with obesity, diabetes and insulin-resistance[22] (Supplementary Fig.7a). Using ontology and network analysis, we further observed global, log-fold, differences in T cell gene expression from DIO versus control mice in genes involved in metabolism,

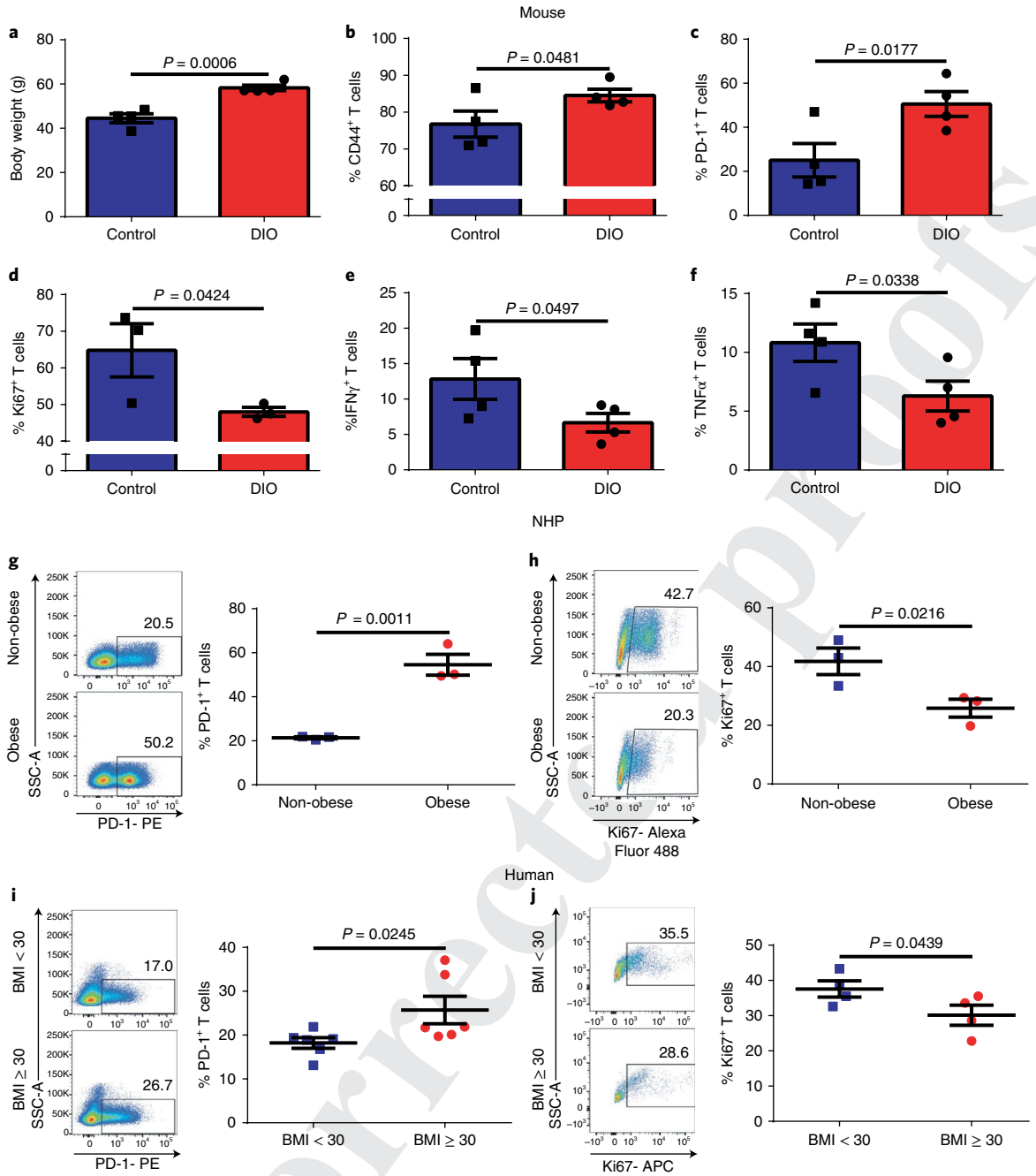

Fig. 1 | Obesity-related T cell dysfunction across multiple species. a, Body weights of 11- to 12-month-old male control and DIO mice ($n = 4$ per group). **b**,**c**, Frequency of (**b**) CD44+ and (**c**) PD-1+ T cells in the liver of 11- to 12-month-old male control and DIO mice ($n = 4$ per group) assessed by flow cytometry. **d**–**f**, Frequency of (**d**) Ki67+ ($n = 3$ per group), (**e**) IFNγ+ ($n = 4$ per group), and (**f**) TNFα+ ($n = 4$ per group) T cells in the liver of 11- to 12-month-old male control and DIO mice after ex vivo stimulation. **g**, Representative flow plots and frequency of PD-1+ T cells in the peripheral blood of non-obese and obese rhesus macaques ($n = 3$ per group). **h**, Representative flow plots and frequency of Ki67-expressing T cells after ex vivo stimulation of rhesus macaque peripheral blood mononuclear cells (PBMCs; $n = 3$ per group). **i**, Representative flow plots and frequency of PD-1+ T cells in the peripheral blood of non-obese (BMI < 30) and obese (BMI ≥ 30) healthy human volunteers ($n = 6$ per group). **j**, Representative flow plots and frequency of Ki67-expressing T cells after ex vivo stimulation of healthy human PBMCs ($n = 4$ per group). Data in this figure are all depicted as mean ± s.e.m., with all individual points shown. One-tailed unpaired Student's *t*-test *P* values are shown.

T cell activation, Toll-like receptor signaling, regulation of chemotaxis and protein folding similarly (Fig. 2i, Benjamini–-Hochberg false discovery rate < 0.05). Similar results were obtained using represented ontologies of either down-regulated (Fig. 2j) or up-regulated genes (Supplementary Fig.7b) through network analysis. These results suggest that T cells from tumor-bearing DIO mice exhibit a transcriptomic profile that is markedly different from that of T cells from tumor-bearing control mice, findings consistent with increased exhaustion and inflammation.

Leptin levels are correlated with PD-1 expression. Obesity has been demonstrated to induce a meta-inflammatory state with increased pro-inflammatory cytokines such as TNFα and IL-6, as well as elevated levels of glucose, insulin, fatty acids and leptin. Leptin, which

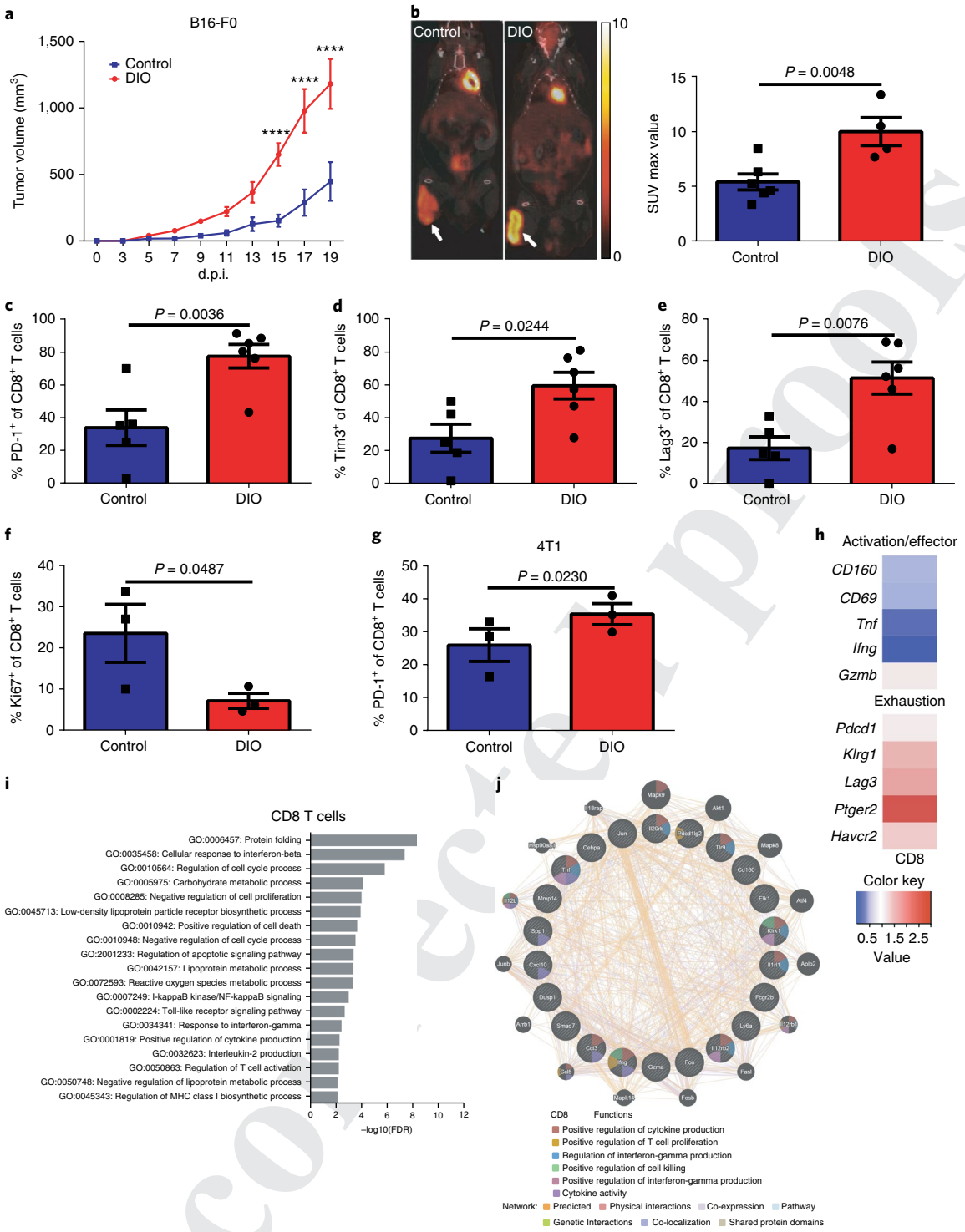

Fig. 2 | Obesity promotes tumor growth and T cell exhaustion. a, Tumor volume of B16-F0 melanoma subcutaneously inoculated in 6-month-old control ($n=4$) and DIO ($n=5$) C57BL/6 male mice. Tumor volumes depicted as mean ± s.e.m. Two-way ANOVA with Tukey post-hoc test P values used. ****$P<0.001$. d.p.i, days post inoculation. **b**, Representative PET-CT images and quantification of tumor burden comparing 6-month-old B16-F0-tumor-bearing control ($n=6$) and DIO ($n=4$) mice 18 d.p.i. **c**,**d**,**e**, Frequency of (**c**) PD-1, (**d**) Tim3, and (**e**) Lag3 on tumor-infiltrating CD8 + T cells from 6-month-old B16-F0-bearing controls ($n=5$) and DIO ($n=6$) male mice at 16 d.p.i. **f**, Frequency of Ki67 on tumor-infiltrating CD8 + T cells from 6-month-old B16-F0-bearing control and DIO male mice ($n=3$ per group). **g**, Frequency of PD-1 on tumor-infiltrating CD8 + T cells from 4T1-bearing control and DIO female mice ($n=3$ per group) at 23 d.p.i. Data in **b**–**g**, are depicted as mean ± s.e.m., with all individual points shown. One-tailed unpaired Student's t-test P values are shown. **h**, Heat maps generated from RNA-seq data showing differentially expressed activation/effector and exhaustion genes (≥1.5-fold difference in CD44+CD8+ T cells isolated from the spleens and lymph nodes of 6-month-old B16-F0-bearing control and DIO C57BL/6 male mice at 16 d.p.i. Data are shown as fold change over controls ($n=3$ per group). **i**, Candidate genes based on false discovery rate cutoff of 1.5-fold change functionally categorized. The most significant pathways of candidate genes were analyzed using G:Profiler by the g:GOST comprehensive method ($P<0.05$) ($n=3$ per group). **j**, Network analysis of down-regulated genes (DIO relative to control) in CD8+ T cells from enriched gene sets using GeneMANIA ($n=3$ per group).

is characteristically present at high levels in obesity, has not been previously linked to PD-1 expression, but studies suggest that it can affect T cell function[25–27]. The RNA sequencing (RNA-seq) analysis on T cells from B16-bearing control and DIO mice revealed differential expression of pathways involved in fat metabolism and T cell signaling and showed marked changes in the expression of genes previously described to be involved with leptin signaling[28] including several IFN-inducible GTPases[29] (Supplementary Fig. 8a). In healthy human volunteers (Supplementary Table 1), we observed significantly increased serum leptin levels in obese donors (Fig. 3a), which correlated with PD-1 expression on CD8+ T cells (Fig. 3b and Supplementary Fig. 8b). Similarly, leptin levels were elevated in DIO mice, and this corresponded with an elevated frequency of PD-1 on CD8+ T cells (Fig. 3c,d and Supplementary Fig. 1e,f). Using ad libitum (AL)-fed mice, which gain weight and visceral adipose tissue as they age, and age-matched calorie restricted (CR) mice, we next determined whether limiting body weight and adipose tissue could minimize leptin levels and T cell exhaustion. CR mice had decreased visceral adiposity compared with AL mice, as measured by magnetic resonance imaging (Fig. 3e), and weighed significantly less and had lower leptin levels (Supplementary Fig. 8c,d). The reduced obesity and leptin levels in CR mice were accompanied by a significantly lower frequency of PD-1+CD8+ T cells in the liver and spleen as well as a lower frequency of Eomes+PD-1+CD8+ T cells (Fig. 3f and Supplementary Fig. 8c–i) demonstrating that reduction of body fat resulted in lower leptin and T cell dysfunction with age. We next examined T cell phenotype in leptin-deficient *ob/ob*[30] and leptin receptor (ObR)-deficient *db/db* mice[31], both of which are obese due to lack of the satiety signal. As expected, *db/db* mice weighed significantly more than age-matched wild type (WT) control mice (Supplementary Fig. 9a), but the frequency of CD8+ T cells expressing PD-1 in *db/db* mice was significantly lower than that in WT control mice (Fig. 3g). The *ob/ob* mice were weight matched to wild-type DIO mice and significantly heavier than WT control mice (Supplementary Fig. 9b). The frequency of CD8+ T cells expressing PD-1 from *ob/ob* mice trended lower than that of DIO mice with a similar weight but trended higher than that of control mice (Supplementary Fig. 9c,d). These results suggest that leptin is not required for PD-1 expression on CD8+ T cells but that in the setting of obesity intact leptin signaling contributes to the PD-1+ phenotype. We next examined the fate of T cells from WT (ObR+) and *db/db* (ObR-) mice on regular diet subject to allogeneic activation by adoptive transfer into immunodeficient but H2-disparate ($H2^d$) NSG mice (Supplementary Fig. 9e). Comparing the number of CD8+ T cells originally transferred into NSG mice to the number of donor cells found in the spleen (Supplementary Fig. 9f) and liver (Supplementary Fig. 9g) at 13 days post transfer, we observed that WT cells expanded minimally in marked contrast with *db/db* T cells, which expanded robustly. This increased expansion of *db/db* CD8+ T cells was associated with lower PD-1 expression (Fig. 3h,i). Comparing PD-1 frequency of transferred cells pre- and post-transfer, we found that both WT and *db/db* CD8+ T cells increased PD-1 expression upon transfer and chronic allogenic stimulation, but the extent of that increase was drastically more pronounced in WT CD8+ T cells, which showed a 40-fold increase in PD-1 expression (Supplementary Fig. 9h). These results suggest that T cells with intact leptin signaling are more susceptible to PD-1 upregulation and proliferative dysfunction with chronic stimulation in vivo whereas leptin unresponsive T cells remain functional with limited PD-1 upregulation.

To further link leptin to PD-1 expression and T cell exhaustion we evaluated in vitro the effects of leptin on T cell activation directly. Mirroring the in vivo results with allogeneic stimulation, PD-1 expression on CD8+ T cells was increased upon stimulation with anti-CD3 (αCD3), and this upregulation was dramatically enhanced with addition of recombinant mouse leptin (rmleptin, Fig. 3j). This addition increased PD-1 expression correlated with upregulation of phospho-STAT3 (pSTAT3; Supplementary Fig. 10a,b), a major downstream mediator of leptin signaling, which is also known to induce PD-1 expression on T cells through distal regulatory elements that interact with the PD-1 gene promoter[32]. Importantly, the addition of a STAT3 inhibitor significantly decreased both the upregulation of pSTAT3 and PD-1 induced by stimulation and leptin (Supplementary Fig. 10a-b). Leptin can increase T cell activation[33,34], and obesity can cause leptin resistance[35,36]. An alternate explanation for the T cell phenotype of DIO mice could be that leptin increases T cell activation, and in obesity, T cells develop leptin resistance. Therefore, we examined the induction of pSTAT3 by leptin stimulation in T cells from control and DIO mice. There were no differences in the expression of pSTAT3 on CD8+ T cells from control and DIO mice (Supplementary Fig. 10c), indicating that CD8+ T cells in DIO mice are not resistant to leptin, in agreement with published reports on DIO mice. Our studies with sorted human T cells in vitro revealed that mitogen-driven proliferation of memory T cells, but not naïve T cells, was inhibited by leptin, also in agreement with previous findings[37] (Supplementary Fig. 10d). Collectively, our findings implicate leptin as a link between obesity and increased PD-1 expression and exhaustion on memory T cells.

We then examined the effect of leptin on T cell exhaustion in tumor-bearing models using leptin-deficient mice. We treated B16-tumor-bearing *ob/ob* mice with rmleptin and examined tumor growth and immune activity (Supplementary Fig. 11a). Although *ob/ob* mice treated with exogenous rmleptin continuously lost weight, tumors in these mice grew faster (Supplementary Fig. 11b,c). Importantly, leptin treatment resulted in increased CD8+ T cell exhaustion in the tumor environment with significantly decreased IFNγ on PD-1+ CD8+ T cells (Fig. 4a), increased numbers of PD-1+CD8+ T cells, decreased expression of Ki67, and significantly increased expression of Eomes at the mRNA level (Supplementary Fig. 11d-f). Exogenous rmleptin also significantly affected CD8 + T cells outside of the TME as demonstrated in the liver. Leptin upregulated PD-1 expression at the mRNA and protein levels (Supplementary Fig. 11g,h), as well as mRNA expression of *HAVCR2* (Tim3) and *Cpt1a* (Supplementary Fig. 11i,j), resulting in diminished proliferation of PD-1 + CD8 + T cells (Fig. 4b). To examine the consequences of obesity and leptin signaling on the anti-tumor immune response, we adoptively transferred T cells from WT (ObR+) or *db/db* mice into control or DIO immune-deficient C57BL/6 $Rag2^{-/-}$ mice, which lack T cells, bearing B16-F0 tumors (Fig. 4c,d and Supplementary Fig. 12a). Consistent with our previous data, tumor growth was accelerated in DIO $Rag2^{-/-}$ mice compared with control $Rag2^{-/-}$ mice (Supplementary Fig. 12b,c) after adoptive transfer of WT T cells. Importantly, Q8 tumor growth kinetics were similar regardless of whether *db/db* T cells were transferred into control or DIO $Rag2^{-/-}$ C57BL/6 mice, whereas tumors grew faster in DIO $Rag2^{-/-}$ mice that received WT T cells compared with control $Rag2^{-/-}$ mice that received WT T cells (Fig. 4e and Supplementary Fig. 12d). This finding suggests that the obese environment, with elevated leptin, impairs the anti-tumor responses of transferred WT CD8+ T cells, but not leptin-resistant *db/db* CD8+ T cells. This is confirmed by TME immunophenotyping, which demonstrates significantly higher expression of PD-1 on WT adoptively transferred CD8 + T cells in DIO $Rag2^{-/-}$ mice versus *db/db* T cells in the DIO $Rag2^{-/-}$ mice or versus WT or *db/db* T cells in control $Rag2^{-/-}$ hosts (Fig. 4f and Supplementary Fig. 12e). Importantly, ex vivo analysis of TNFα and IFNγ production also demonstrated improved functionality of *db/db* TILs (compared with WT TILS) isolated from the TME of DIO Rag2–/– mice, whereas WT and *db/db* TILs from tumors in control $Rag2^{-/-}$ had equivalent functionality (Fig. 4g–i and Supplementary Fig. 12f–h). These results indicate a role of leptin signaling in increasing PD-1 expression and promoting T cell exhaustion in tumor-bearing mice, which affects anti-tumor immunity.

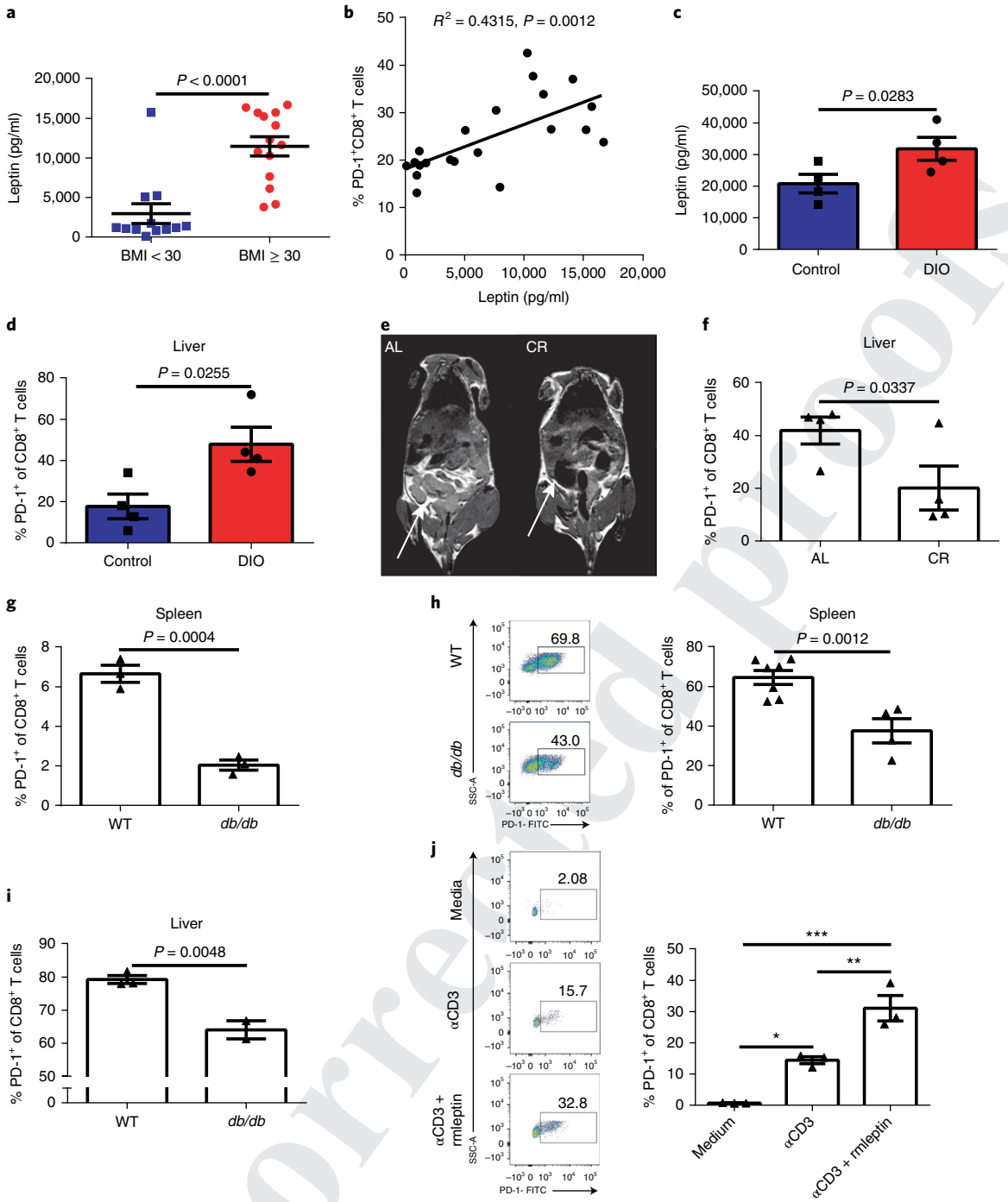

Fig. 3 | Leptin level is correlated with PD-1 expression. a, Leptin levels in non-obese (BMI < 30, $n = 14$) and obese (BMI ≥ 30, $n = 12$) healthy human volunteers. **b**, Linear regression analysis of leptin levels and PD-1 expression on CD8+ T cells in peripheral blood of human volunteers ($n = 21$). **c**,**d** Leptin levels (**c**) and PD-1 expression (**d**) on liver CD8+ T cells in 11- to 12-month-old control and DIO male mice ($n = 4$ per group). **e**, T1-weighted MRI demonstrating subcutaneous and visceral fat (fat appears bright white, white arrows) in 19-month-old AL-fed and age-matched CR male mice. **f**, Frequency of PD-1 expressing CD8+ T cells in the liver of 19-month-old AL and CR male mice ($n = 4$ per group). **g**, Frequency of PD-1+CD8+ T cells from spleens of WT and *db/db* (9-month-old) male mice ($n = 3$ per group). **h**,**i**, Representative flow plots and frequency of PD-1 on (**h**) splenic ($n = 7$ in WT group, $n = 4$ in *db/db* group) and (**i**) liver ($n = 3$ in WT group, $n = 2$ in *db/db* group) CD8+ T cells of NSG mice 13 days post-transfer. Data in **a**,**c**,**d**,**f**–**i** are depicted as mean ± s.e.m., with all individual points shown. One-tailed unpaired Student's *t*-test *P* values are shown. **j**, Representative flow plots and frequency of PD-1 expression on splenic CD8+ T cells ex vivo stimulated with αCD3, αCD3 and recombinant mouse leptin (αCD3+rmleptin), or unstimulated for 24 h ($n = 3$ technical replicates). Data are depicted as mean ± s.e.m., with all individual points shown. One-way ANOVA with Tukey post-hoc test were used to compare groups. $^*P < 0.05$, $^{**}P < 0.01$, $^{***}P < 0.001$.

Improved efficacy of PD-1 checkpoint blockade in DIO mice. Building on our observations that CD8+ T cells have increased exhaustion and dysfunction in obese, cancer-bearing subjects, we assessed the impact of PD-1 blockade on tumor growth. Administration of anti-PD-1 (αPD-1) as a monotherapy (Supplementary Fig. 13a) had minimal to no effect on control mice but surprisingly led to significant

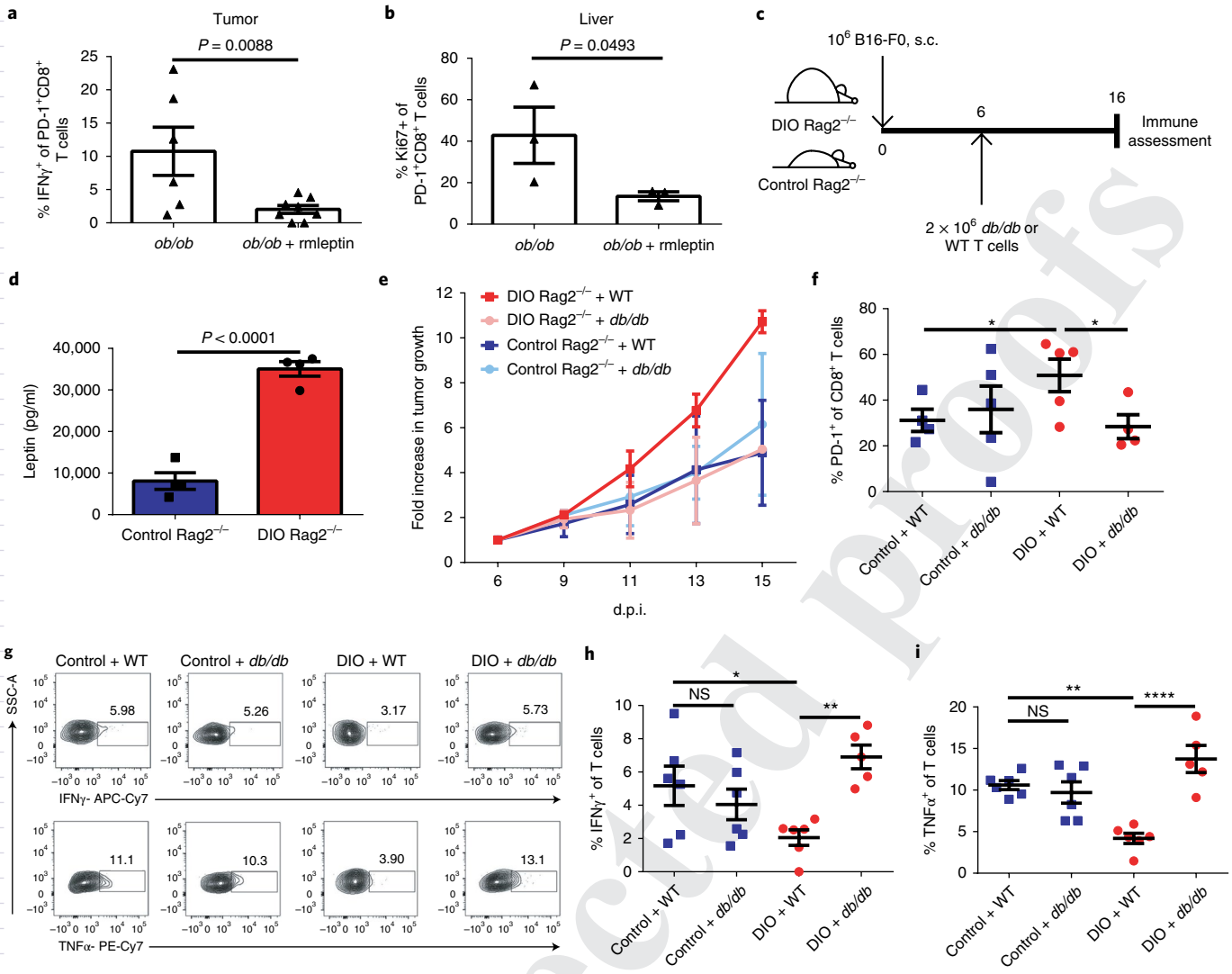

Fig. 4 | Lack of leptin signaling rescues T cells from exhaustion in obese mice. a, Frequency of IFNγ+ tumor-infiltrating CD8+PD-1+ T cells after ex vivo stimulation ($n=3$ per group, two technical replicates in *ob/ob* group, two to three technical replicates in *ob/ob* + rmleptin group). **b**, frequency of Ki67 in CD8+PD-1+ T cells in the liver of 3-month-old *ob/ob* male B16-F0-bearing mice treated with or without rmleptin ($n=3$ per group). **c**, Schema of C57BL/6 Rag2$^{-/-}$ mice challenged with B16 melanoma cells followed by adoptive transfer of T cells from either WT or *db/db* C57BL/6 mice. s.c., subcutaneous. **d**, Serum leptin levels of 5-month-old control and DIO C57BL/6 Rag2$^{-/-}$ male mice ($n=4$ per group). Data in **a**,**b**,**d** are depicted as mean ± s.e.m., with all individual points shown. One-tailed unpaired Student's *t*-test was used to compare groups. **e**, Fold change of B16-F0 tumor growth in control and DIO Rag2$^{-/-}$ mice after adoptive transfer of T cells from either WT or *db/db* C57BL/6 mice (fold change compared to tumor size at time of adoptive transfer) ($n=2$ per group). **f**, Frequency of PD-1 expression on tumor-infiltrating CD8+ T cells from B16-F0-bearing control ($n=4$ in WT group, $n=5$ in *db/db* group) and DIO ($n=5$ in WT group, $n=4$ in *db/db* group) Rag2$^{-/-}$ mice with adoptive transfer of T cells from either WT or *db/db* C57BL/6 mice. **g**,**h**,**i**, Representative flow staining (**g**) and frequency of IFNγ- (**h**) and TNFα- (**i**) producing tumor-infiltrating T cells after ex vivo stimulation collected from B16-F0-bearing control and DIO Rag2$^{-/-}$ mice with adoptive transfer of T cells from either WT or *db/db* mice ($n=2$ per group, two or three technical replicates). Data in **f**,**h**,**i**, are depicted as mean ± s.e.m., with all individual points shown. One-way ANOVA with Tukey post-hoc test was used to compare groups. $^{*}P<0.05$, $^{**}P<0.01$, $^{****}P<0.001$. NS, not significant.

and marked reduction in B16 tumor burden and a significant improvement in survival in DIO mice (Fig. 5a,b and Supplementary Fig. 13b,c). Similar results were also observed in 3LL-tumor-bearing DIO mice (Fig. 5c and Supplementary Fig. 13d,e). Of note, in agreement with our other models demonstrating accelerated tumor growth in obese models, 3LL tumors also grew faster in DIO mice. These results demonstrate that in models in which αPD-1 monotherapy has limited effect (B16)[38] or where there is some susceptibility to monotherapy (3LL)[39], DIO mice displayed significantly greater therapeutic efficacy than control recipients. The improved responsiveness in DIO mice was associated with a significant increase in the total number of tumor-infiltrating T cells and increased frequency of CD8+ T cells in the TME (Fig. 5d,e and Supplementary Fig. 13f,g), as well as an increased CD8-to-CD4 T cell ratio (Supplementary Fig. 13h) in response to therapy. In DIO mice, αPD-1 therapy also reduced the frequency of PD-1+ T cells in the TME (Supplementary Fig. 13i,j). Similarly, ex vivo functional assessment of splenic CD8+ T cells from αPD-1-treated tumor-bearing DIO mice demonstrated significantly increased TNFα and IFNγ production on CD8+ T cells, compared with controls (Supplementary Fig. 14a,b). Overall, αPD-1 therapy rescued CD8+ T cells from exhaustion and significantly improved survival

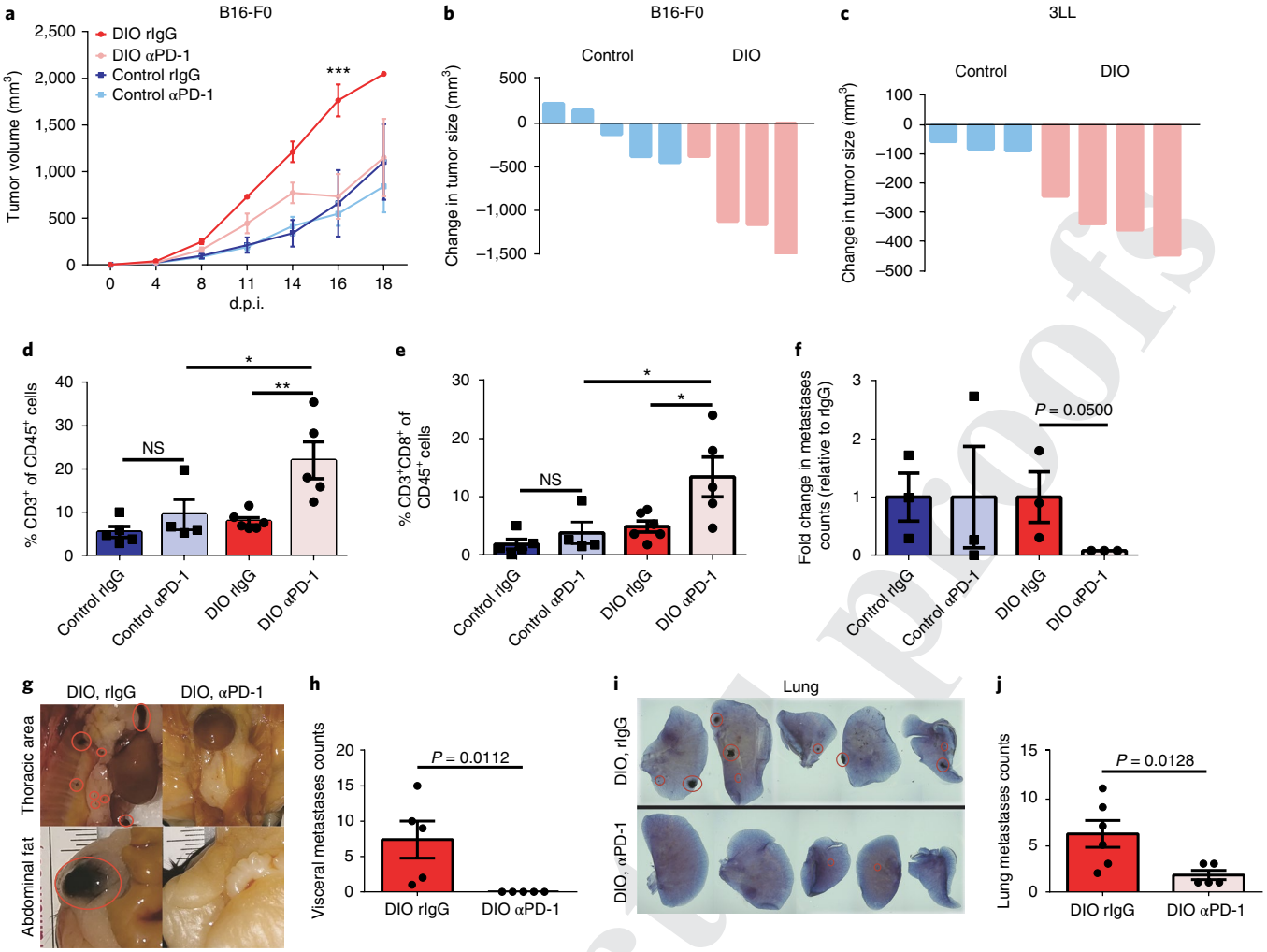

Fig. 5 | Improved efficacy of aPD-1 treatment in DIO mice. a, Volume of B16-F0 melanoma in 6-month-old control and DIO C57BL/6 male mice with and without αPD-1 treatment ($n=4$ in control and DIO rIgG groups, $n=5$ in control and DIO αPD-1 groups). Tumor volumes are depicted as mean ± s.e.m. Two-way ANOVA with Tukey post-hoc test was used to compare groups. **b**,**c**, Waterfall plots of the volumes of (**b**) B16-F0 ($n=5$ in control group, $n=4$ in DIO group) at 16 d.p.i. and (**c**) 3LL lung carcinoma ($n=3$ in control group, $n=4$ in DIO group) 11 d.p.i. in 6-month-old control and DIO C57BL/6 male mice with and without αPD-1 treatment (graphed as change in tumor volume compared to non-treatment controls). **d**,**e**, Frequency of tumor-infiltrating (**d**) CD3+ cells and (**e**) CD8+ T cells as a percentage of CD45+ cells in the tumor ($n=6$ in DIO rIgG group, $n=5$ in control rIgG and DIO αPD-1 groups, $n=4$ in control αPD-1 group). Data are depicted as mean ± s.e.m., with all individual points shown. One-way ANOVA with Tukey post-hoc test was used to compare groups. **f**, Fold change of total metastases in intravenously injected B16-F10-bearing control and DIO mice with and without αPD-1 treatment (graphed as change in tumor metastases counts compared to non-treatment controls) at 28 d.p.i. ($n=3$ per group). Data are depicted as mean ± s.e.m., with all individual points shown. Mann–Whitney test was used to compare DIO rIgG and αPD-1 groups. **g**,**h**, Representative pictures (**g**) and quantification (**h**) of metastases in visceral fat of non-treated and treated B16-F10-bearing DIO mice ($n=5$ per group). Data are depicted as mean ± s.e.m., with all individual points shown. One-tailed unpaired Student's *t*-test *P* values are shown. **i**,**j**, Representative staining (**i**) and quantification (**j**) of lung metastases in non-treated and treated B16-F10-bearing DIO mice ($n=6$ in rIgG group, $n=5$ in αPD-1 group). Data are depicted as mean ± s.e.m., with all individual points shown. One-tailed unpaired Student's *t*-test *P* values shown. $^{*}P<0.05$, $^{**}P<0.01$, $^{***}P<0.005$; NS, not significant.

in DIO mice. Similar anti-tumor effects were also observed in a melanoma metastasis model (B16-F10, Supplementary Fig. 14c). Importantly, αPD-1 treatment significantly inhibited metastases in B16-bearing DIO mice, but not in control mice (Fig. 5f). Further examination of the effects of αPD-1 in DIO mice revealed significant inhibition of both visceral and lung metastases (Fig. 5g–j). Importantly, despite the risks of severe or lethal toxicities after systemic immune-stimulatory therapies in obese mice[40], adverse events were not observed after αPD-1 checkpoint blockade (Supplementary Fig. 14d–g), thus implying an uncoupling of heightened treatment response and risk of toxicity in the setting of obesity that may be contingent on the type of immunotherapy applied.

Impact of obesity on PD-1 expression and effects of checkpoint blockade in obese cancer patients. Because significant anti-tumor effects were observed with αPD-1 therapy in obese mouse models, we examined T cell phenotypes in the TME of obese human cancer patients. In a large cohort of 152 human colorectal cancers, we observed significantly fewer tumor-infiltrating-T cells in obese patients (Fig. 6a, b). Because patients with CRC have a poor response rate to checkpoint blockade, we also examined a more responsive tumor type: melanoma. In a cohort of 251 patients with melanoma with annotated clinical data from the cancer genome atlas (TCGA) a 1.57-fold ($P=0.019$) increase in mean PD-1 expression was noted in tumors of obese patients (BMI ≥ 30) (data not shown). Among

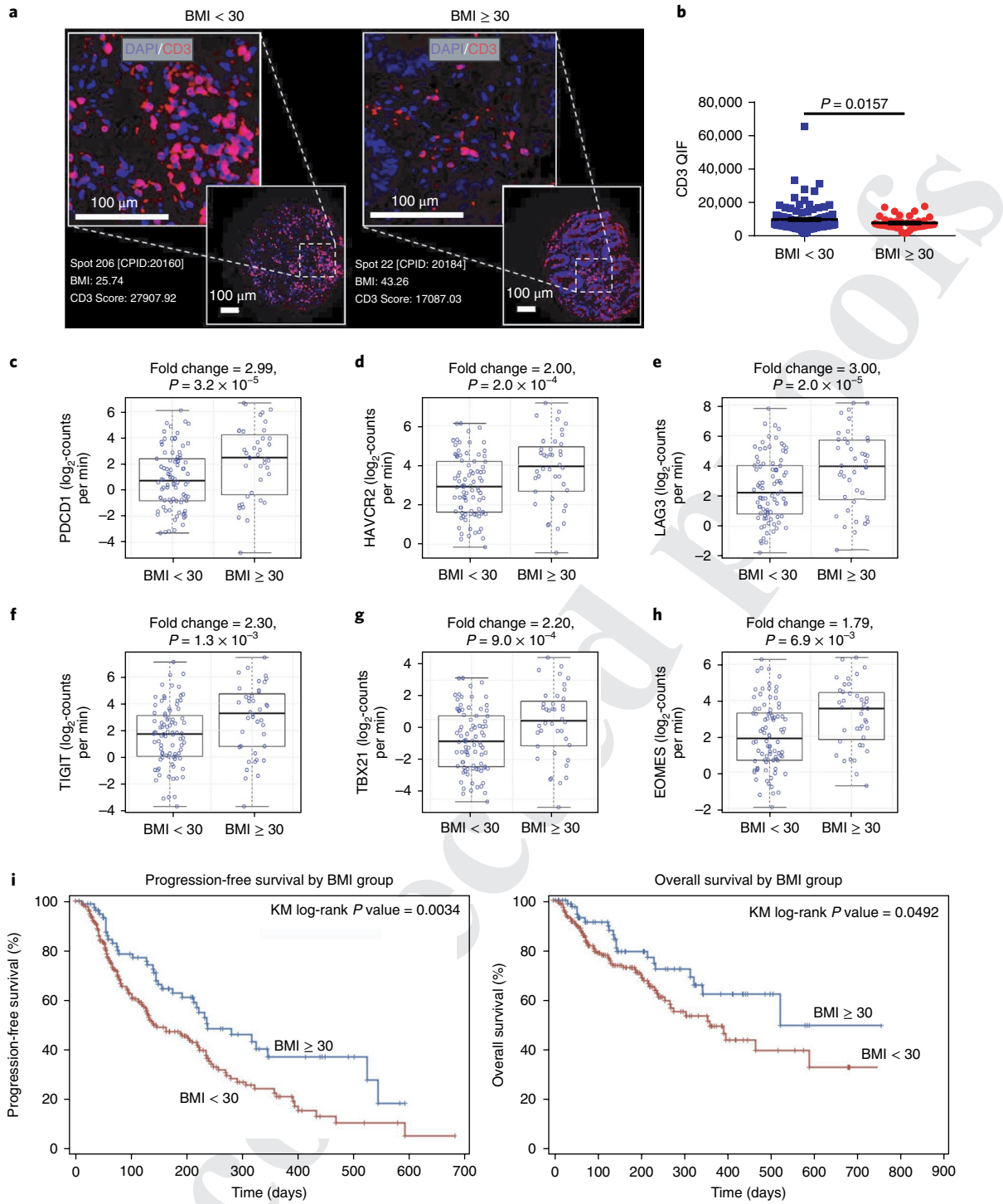

Fig. 6 | T cell profile and improved efficacy of aPD-(L)1 immunotherapy in obese cancer patients. a,**b**, Representative immunofluorescent staining (**a**) and bar graph (**b**) of CD3+ infiltrates in the TME of human colorectal cancers ($n = 113$ in BMI < 30 group, $n = 39$ in BMI ≥ 30 group). Data are depicted as mean ± s.e.m., with all individual points shown. One-tailed unpaired Student's *t*-test *P* values are shown. **c**–**h**, Human TCGA data analysis of (**c**) PDCD1 (PD-1), (**d**) HAVCR2 (Tim3), (**e**) LAG3, (**f**) TIGIT, (**g**) TBX21 (T-bet), and (**h**) EOMES expression in melanoma tumors in non-obese ($n = 86$) versus obese ($n = 40$) patients. The line midline of each box represents the median. The lower and upper boundaries of the box indicate first and third quartiles, respectively. The whiskers indicate the minimum and maximum values. *P* values calculated via DESeq2 (Wald-Test) to compare groups. (**i**) PFS and (**j**) OS of 250 human cancer patients treated with PD-(L)1 checkpoint blockade and stratified by BMI ($n = 169$ in BMI < 30, $n = 81$ in BMI > = 30). **i**,**j**, Kaplan–Meier (KM) estimates of PFS and OS.

patients older than 60 years of age ($n = 126$), the effect of obesity on exhaustion marker expression in the TME was even more pronounced with a threefold increase in PDCD1 (PD-1) in obese patients (Fig. 6c, $P = 3.2 \times 10^{-5}$), twofold increase in HAVCR2 (Tim3) (Fig. 6d, $P = 2.0 \times 10^{-4}$), threefold increase in LAG3 (Fig. 6e, $P = 2.0 \times 10^{-5}$), 2.3-fold increase in TIGIT (Fig. 6f, $P = 1.3 \times 10^{-3}$),

2.2-fold increase in TBX21 (T-bet) (Fig. 6g, $P=9.0\times10^{-4}$), and 1.79-fold increase in EOMES (Fig. 6h, $P=6.9\times10^{-3}$). These results generally mirrored the TME phenotype in DIO mouse tumors, with no change in FOXP3, leptin receptor, CTLA-4 and CD274 (PD-L1) expression (Supplementary Fig. 15a–d). Most importantly, we observed a striking improvement in the clinical outcomes of obese (BMI ≥ 30) versus non-obese (BMI < 30) patients, in a cohort of 250 human patients treated with αPD-(L)1 checkpoint blockade for a variety of cancers (Supplementary Table 2). There was a statistically significant improvement in progression-free survival (median: 237 versus 141 days, $P=0.0034$) and overall survival (median: 523 versus 361 days, $P=0.0492$) in obese patients (Fig. 6i,j). As in obese mice, no increases in immune-related adverse effects were observed in obese patients (Supplementary Table 2). Using a Cox proportional hazards model to adjust for ECOG performance status, line of treatment, age, sex and cancer type, BMI category was still significantly associated with better progression-free survival (HR = 0.61, 95% CI = 0.42–0.89, $P=0.01$) and overall survival after αPD-(L)1 therapy (HR = 0.594, 95% CI = 0.35–0.99, $P=0.048$).

Discussion

In this report, we demonstrate for the first time, across multiple species and tumor models, that obesity increases T cell aging resulting in higher PD-1 expression and dysfunction, which is driven, at least in part, by leptin signaling. We also observed increased tumor progression in the setting of obesity, and this was probably due to immunosuppression as well as direct (metabolic and hormonal[41]) effects. However, the PD-1-mediated T cell dysfunction in obesity remarkably left tumors markedly more responsive to checkpoint blockade. Importantly, these preclinical findings are corroborated by clinical data demonstrating significantly improved outcomes in obese cancer patients treated with PD-1/PD-L1 inhibitors.

Our findings validate and provide a mechanism for a recent report in obese melanoma patients showing improved outcomes with immunotherapy[14]. In that study, the effect was limited to male melanoma patients, whereas our clinical data extend across cancer types and demonstrates a positive effect even when controlling for sex. Although our study focuses on PD-1-mediated T cell dysfunction induced by obesity, sex and other factors such as age, genetics, metabolic dysregulation, gut microbiome, dietary differences and the duration of obesity probably confound the effects of obesity on the immune system and warrant further study. Age in particular is known to increase the memory pool of T cells and may be a key confounder particularly in specific-pathogen-free laboratory mice, which experience limited exposure to immune challenges. In our studies 6-month-old DIO mice did not display the heightened phenotypic exhaustion seen in 11-month-old DIO mice, unless challenged with a tumor. This finding is consistent with the concept that obesity results in an immune aging effect, termed inflammaging[12], which is accentuated by immune challenge. Thus, age, sex, exposure to immune challenge and obesity may all play critical roles in shaping immune responses. Furthermore, obesity probably operates via multiple pathways aside from the PD-(L)1 axis to induce T cell dysfunction and promote tumor growth, and these phenomena are likely also influenced by diet. We observed elevated *Cpt1a* expression, a master regulator of fatty acid oxidation and driver of metabolic changes leading to exhaustion[18]. Other factors associated with obesity, such as free fatty acids, insulin/IGF1, and proinflammatory cytokines such as TNF and IL6, all are likely to contribute to this phenotype outside of body fat. As a result, it will be important to ascertain the effects of different diets and duration of exposure needed to observe possible immune-altering effects.

In our study, tumor-bearing DIO mice showed higher expression of Eomes than T-bet, which supports an exhausted CD8+ T cell profile[4,42]. Although some studies suggest that T-bet^{hi} but not Eomes^{hi} exhausted T cells respond better to PD-1 blockade[4], it has been demonstrated that blocking the PD-(L)1 axis can reinvigorate PD-1^{hi}T-bet^{lo}Eomes+CD8+ T cells[43].

We focused on leptin as a mechanism of obesity-induced T cell dysfunction, given that STAT3, a major downstream transcription factor of the leptin receptor[44,45], has known binding sites in the promoter region of PD-1[46,47] and has been implicated in driving expression of PD-1 in human and murine cancers[48]. However, it is important to recognize that these molecules have broad pleiotropic effects, and other pathways are probably implicated. This notion was demonstrated by the effects of administering leptin to *ob/ob* mice, where significant metabolic effects also occurred.

While leptin has been well documented to impact T cells, particularly Tregs, the literature also suggests that leptin increases T cell activation[26,34], which may be explained by the opposing effects of leptin on naïve versus memory T cell populations as previously reported[37]. PD-1 plays critical roles both in early T cell activation as well as in later chronic stimulation, where the exhaustion phenotype predominates. Thus, differences between our findings and others are likely to be explained by the T cell populations examined and the time points assessed. The impact of leptin and obesity on other immune cells is also likely to be important, given the recent report linking leptin in tumor-bearing DIO mice with PD-L1 expression in myeloid-derived suppressor cells[49]. Our results also suggest that targeting the leptin receptor on activated T cells or CAR T cells in immunotherapy may be of use to augment T cell function, particularly in high-leptin circumstances.

Overall, our data suggest that obesity-associated inflammaging results in increased T cell aging and induction of normal suppressive pathways to counter this chronic inflammatory state. In obesity, PD-1-mediated immune suppression may be a mechanism to protect against possible autoreactive or hyperactive T cell responses induced by chronic inflammation. Importantly, the linkage of obesity and leptin to PD-1 and T cell dysfunction in cancer progression appears remarkably robust in both mouse and human studies. It remains to be determined whether obesity increases PD-1+ CD8 T cells in a broad range of human cancers and whether this mechanism also contributes to the increased incidence of cancer in obese patients. Furthermore, it remains to be delineated clinically whether the environment in the obese state results in greater T cell activation and function once checkpoint blockade is applied. It is unclear if obesity may impact the survival of cancer patients by other non-immune factors as well. In that regard, obesity should not necessarily be regarded as a positive prognostic factor in cancer but rather as a potential mediator of immune dysfunction and tumor progression that can be successfully reversed by PD-(L)1 checkpoint inhibition resulting in heightened efficacy.

Online content

Any methods, additional references, Nature Research reporting summaries, source data, statements of data availability and associated accession codes are available at [https://doi.org/10.1038/s41591-018-0221-5]

Received: 25 September 2017; Accepted: 12 September 2018;

References

1. Robert, C. et al. Pembrolizumab versus ipilimumab in advanced melanoma. *N. Engl. J. Med.* **372**, 2521–2532 (2015).
2. Garon, E. B. et al. Pembrolizumab for the treatment of non-small-cell lung cancer. *N. Engl. J. Med.* **372**, 2018–2028 (2015).
3. Powles, T. et al. MPDL3280A (anti-PD-L1) treatment leads to clinical activity in metastatic bladder cancer. *Nature* **515**, 558–562 (2014).
4. Wherry, E. J. & Kurachi, M. Molecular and cellular insights into T cell exhaustion. *Nat. Rev. Immunol.* **15**, 486–499 (2015).
5. Barber, D. L. et al. Restoring function in exhausted CD8 T cells during chronic viral infection. *Nature* **439**, 682–687 (2006).

6. Blackburn, S. D. et al. Coregulation of CD8+T cell exhaustion by multiple inhibitory receptors during chronic viral infection. *Nat. Immunol.* **10**, 29–37 (2009).
7. Velu, V. et al. Enhancing SIV-specific immunity in vivo by PD-1 blockade. *Nature* **458**, 206–210 (2009).
8. Twyman-Saint Victor, C. et al. Radiation and dual checkpoint blockade activate non-redundant immune mechanisms in cancer. *Nature* **520**, 373–377 (2015).
9. Mehnert, J. M. et al. The challenge for development of valuable immuno-oncology biomarkers. *Clin. Cancer Res.* **23**, 4970–4979 (2017).
10. Tao, W. & Lagergren, J. Clinical management of obese patients with cancer. *Nat. Rev. Clin. Oncol.* **10**, 519–533 (2013).
11. Deng, T., Lyon, C. J., Bergin, S., Caligiuri, M. A. & Hsueh, W. A. Obesity, inflammation, and cancer. *Annu. Rev. Pathol.* **11**, 421–449 (2016).
12. Hotamisligil, G. S. Inflammation and metabolic disorders. *Nature* **444**, 860–867 (2006).
13. Cawley, J. & Meyerhoefer, C. The medical care costs of obesity: an instrumental variables approach. *J. Health Econ.* **31**, 219–230 (2012).
14. McQuade, J. L. et al. Association of body-mass index and outcomes in patients with metastatic melanoma treated with targeted therapy, immunotherapy, or chemotherapy: a retrospective, multicohort analysis. *Lancet Oncol.* (2018).
15. Albiges, L. et al. Body mass index and metastatic renal cell carcinoma: clinical and biological correlations. *J. Clin. Oncol.* **34**, 3655–3663 (2016).
16. Nunez, N. P. et al. Obesity accelerates mouse mammary tumor growth in the absence of ovarian hormones. *Nutr. Cancer* **60**, 534–541 (2008).
17. Deiuliis, J. et al. Visceral adipose inflammation in obesity is associated with critical alterations in tregulatory cell numbers. *PLoS One* **6**, e16376 (2011).
18. Bengsch, B. et al. Bioenergetic insufficiencies due to metabolic alterations regulated by the inhibitory receptor PD-1 are an early driver of CD8(+) T cell exhaustion. *Immunity* **45**, 358–373 (2016).
19. Buggert, M. et al. T-bet and Eomes are differentially linked to the exhausted phenotype of CD8+T cells in HIV infection. *PLoS. Pathog.* **10**, e1004251 (2014).
20. Crawford, A. et al. Molecular and transcriptional basis of CD4+T cell dysfunction during chronic infection. *Immunity* **40**, 289–302 (2014).
21. Kao, C. et al. Transcription factor T-bet represses expression of the inhibitory receptor PD-1 and sustains virus-specific CD8+T cell responses during chronic infection. *Nat. Immunol.* **12**, 663 (2011).
22. Shirakawa, K. et al. Obesity accelerates T cell senescence in murine visceral adipose tissue. *J. Clin. Invest.* **126**, 4626–4639 (2016).
23. Wherry, E. J. et al. Molecular signature of CD8+T cell exhaustion during chronic viral infection. *Immunity* **27**, 670–684 (2007).
24. Crespo, J., Sun, H., Welling, T. H., Tian, Z. & Zou, W. T cell anergy, exhaustion, senescence, and stemness in the tumor microenvironment. *Curr. Opin. Immunol.* **25**, 214–221 (2013).
25. Naylor, C. & Petri, W. A. Jr Leptin regulation of immune responses. *Trends Mol. Med.* **22**, 88–98 (2016).
26. Saucillo, D. C., Gerriets, V. A., Sheng, J., Rathmell, J. C. & MacIver, N. J. Leptin metabolically licenses T cells for activation to link nutrition and immunity. *J Immunol.* **192**, 136–144 (2014).
27. Lord, G. M. et al. Leptin modulates the T-cell immune response and reverses starvation-induced immunosuppression. *Nature* **394**, 897–901 (1998).
28. Mori, H. et al. Socs3 deficiency in the brain elevates leptin sensitivity and confers resistance to diet-induced obesity. *Nat. Med.* **10**, 739–743 (2004).
29. Liu, B. et al. Irgm1-deficient mice exhibit Paneth cell abnormalities and increased susceptibility to acute intestinal inflammation. *Am. J. Physiol. Gastrointest. Liver Physiol.* **305**, G573–G584 (2013).
30. Halaas, J. L. et al. Weight-reducing effects of the plasma protein encoded by the obese gene. *Science* **269**, 543–546 (1995).
31. Lee, G.-H. et al. Abnormal splicing of the leptin receptor in diabetic mice. *Nature* **379**, 632–635 (1996).
32. Chinai, J. M. et al. New immunotherapies targeting the PD-1 pathway. *Trends Pharmacol. Sci.* **36**, 587–595 (2015).
33. Saucillo, D. C., Gerriets, V. A., Sheng, J., Rathmell, J. C. & MacIver, N. J. Leptin metabolically licenses T cells for activation to link nutrition and immunity. *J. Immunol.* **192**, 136–144 (2014).
34. Lord, G. M. et al. Leptin modulates the T-cell immune response and reverses starvation-induced immunosuppression. *Nature* **394**, 897–901 (1998).
35. Lee, J. H., Reed, D. R. & Price, R. A. Leptin resistance is associated with extreme obesity and aggregates in families. *Int. J. Obesity Relat. Metab. Disord.* **25**, 1471–1473 (2001).
36. Myers, M. G., Leibel, R. L., Seeley, R. J. & Schwartz, M. W. Obesity and leptin resistance: distinguishing cause from effect. *Trends Endocrinol Metab.* **21**, 643–651 (2010).
37. Lord, G. M., Matarese, G., Howard, J. K., Bloom, S. R. & Lechler, R. I. Leptin inhibits the anti-CD3-driven proliferation of peripheral blood T cells but enhances the production of proinflammatory cytokines. *J Leukoc. Biol.* **72**, 330–338 (2002).
38. Kleffel, S. et al. Melanoma cell-intrinsic PD-1 receptor functions promote tumor growth. *Cell* **162**, 1242–1256 (2015).
39. Li, H. Y. et al. The tumor microenvironment regulates sensitivity of murine lung tumors to PD-1/PD-L1 antibody blockade. *Cancer Immunol Res.* **5**, 767–777 (2017).
40. Mirsoian, A. et al. Adiposity induces lethal cytokine storm after systemic administration of stimulatory immunotherapy regimens in aged mice. *J. Exp. Med.* **211**, 2373–2383 (2014).
41. Amjadi, F., Javanmard, S. H., Zarkesh-Esfahani, H., Khazaei, M. & Narimani, M. Leptin promotes melanoma tumor growth in mice related to increasing circulating endothelial progenitor cells numbers and plasma NO production. *J. Exp. Clin. Canc. Res.* **30**, https://doi.org/10.1186/1756-9966-30-21 (2011).
42. Paley, M. A. et al. Progenitor and terminal subsets of CD8+T cells cooperate to contain chronic viral infection. *Science* **338**, 1220–1225 (2012).
43. Utzschneider, D. T. et al. T cell factor 1-expressing memory-like CD8+T cells sustain the immune response to chronic viral infections. *Immunity* **45**, 415–427 (2016).
44. Bates, S. H. et al. STAT3 signalling is required for leptin regulation of energy balance but not reproduction. *Nature* **421**, 856–859 (2003).
45. Buettner, C. et al. Critical role of STAT3 in leptin's metabolic actions. *Cell. Metab.* **4**, 49–60 (2006).
46. Austin, J. W., Lu, P., Majumder, P., Ahmed, R. & Boss, J. M. STAT3, STAT4, NFATc1, and CTCF regulate PD-1 through multiple novel regulatory regions in murine T cells. *J. Immunol.* **192**, 4876–4886 (2014).
47. Bally, A. P. R., Austin, J. W. & Boss, J. M. Genetic and epigenetic regulation of PD-1 Expression. *J. Immunol.* **196**, 2431–2437 (2016).
48. Bu, L. L. et al. STAT3 Induces Immunosuppression by upregulating PD-1/PD-L1 in HNSCC. *J. Dent. Res.* **96**, 1027–1034 (2017).
49. Clements, V. K. et al. Frontline Science: High fat diet and leptin promote tumor progression by inducing myeloid-derived suppressor cells. *J. Leukoc. Biol.* **103**, 395–407 (2018).

Acknowledgements

We would like to thank W. Ma and M. Metcalf from the Murphy lab, D. Rowland, A. Chaudhari and Z. Harmany from the UC Davis CMGI, and J. Chen in the UC Davis Pathology Core for their technical expertise and help. We would also like to thank the other members in the Murphy lab for providing feedback and suggestions during preparation of the manuscript. This was work funded by NIH grant R01 CA095572, R01 CA195904, R01 CA214048, P01 CA065493, R01 HL085794, the California National Primate Research Center base operating grant (OD011107), the UC Davis Comprehensive Cancer Center Support Grant (CCSG) (P30 CA093373), and the UC Davis Mouse Metabolic Phenotyping Center (MMPC) grant (DK092993). The content of this publication does not necessarily reflect the view or policies of the Department of Health and Human Services, nor does mention of trade names, commercial products, or organizations imply endorsement by the U.S. Government. This research was supported in part by the Intramural Research Program of the NIH, NCI, NHLBI and Center for Cancer Research.

Author Contributions

Murine studies: Z.W., E.G.A., J.I.L., A.M., C.T.L., L.T.K., C.D., C.M.M., K.M.S., I.R.S., S.K.G., A.S., A.M.M. Murine studies data analysis/interpretation: Z.W., E.G.A., J.I.L., A.M., C.T.L., L.T.K., C.D., C.M.M., K.M.S., I.R.S., T.S.G., D.L.L., B.R.B., R.J.C., W.J.M., A.M.M. Primate Studies: D.J.H.-O'C., G.M.-L., A.F.T. Human blood donor studies: Z.W., A.M.M., K.K. Human Multiplex IF: K.A.S. TCGA analysis: A.M., E.M. Clinical study: R.A., S.I., S.M., M.M., S.K.V. Overall Study Conception: W.J.M. Overall Study Design: W.J.M., A.M.M. Overall study supervision: W.J.M., A.M.M. Manuscript preparation: Z.W., E.G.A., R.J.C., W.J.M, A.M.M. Manuscript critical review: Z.W., E.G.A., J.I.L., A.M., C.T.L., L.T.K., C.D., C.M.M., K.M.S., I.R.S., S.K.G., S.S.W., R.B.R., D.J.H.-O'C., G.M.-L., A.F.T., R.R.I., T.S.G., K.A.S., A.M., E.M., R.A., S.I., S.M., M.M., S.K.V., D.L.L., B.R.B., R.C., K.K.

Competing Interests Statement

The authors have no competing interests to declare.

Additional information

Supplementary information is available for this paper at https://doi.org/10.1038/s41591-018-0221-5.

Reprints and permissions information is available at www.nature.com/reprints.

Correspondence and requests for materials should be addressed to W.J.M.

Publisher's note: Springer Nature remains neutral with regard to jurisdictional claims in published maps and institutional affiliations.

Methods

Further information on research design is available in the Nature Research Reporting Summary linked to this article.

Mice. Mice were housed in AAALAC-accredited animal facilities at UC Davis under specific-pathogen-free conditions. Protocols were approved by UC Davis IACUC and studies complied with ethical regulations and humane endpoints. Male and female C57BL/6NTac, female BALB/cAnNTac and male B6.129S6-Rag2^{tm1Fwa} N12 (Rag2$^{-/-}$) mice were purchased from Taconic Farms at 4 weeks of age. DDIO and control mice were generated by feeding mice with an open-source purified diet consisting of either 60% fat or 10% fat (D12492 & D12450J, Research Diets, Inc), respectively, starting when the mice were 6 weeks old. Four- to eight-week-old male B6.Cg-Lep^{ob}/J (*ob/ob*) mice and female B6.BKS(D)-Lepr^{db}/J (B6 *db/db*) and WT C57BL/6 mice were purchased from Jackson Laboratory. *ob/ob* mice were used when they were 3–5 months old and equivalent in weight to 9-month-old DIO mice. Six- to nine-month-old BKS.Cg-Dock7^{m}+/+Lepr^{db}/J (BSK *db/db*) were kind gifts from R. R. Isseroff. The female NSG mice (4–5 months old) were kind gifts from J. Nolta. 19-month-old AL and calorie restricted (CR) C57BL/6 mice were obtained from the National Institute on Aging and were fed NIH31 regular chow with a 40% calorie restriction regimen previously published[40].

Leptin and glucose measurements. Leptin concentrations of human plasma were measured using a sandwich ELISA kit from MilliporeSigma. Mouse serum leptin was measured using an electrochemiluminescent assay from Meso Scale Discovery. Mouse glucose was measured using an enzymatic assay from Fisher Diagnostics.

Tumor cell line and treatment. The murine melanoma cell lines B16-F0 (CRL6322™) and B16-F10 (CRL-6475™), Lewis lung carcinoma (3LL, CRL-1642™), and breast cancer 4T1 (CRL-2539™) were obtained from the American Type Culture Collection. C57BL/6 mice were injected subcutaneously in the right flank with 1×10^6 B16-F0 or 3LL tumor cells in 100 µL PBS. BALB/c mice were injected subcutaneously in the right mammary pad with 2×10^5 4T1 tumor cells in 100 µL PBS. Tumor growth was monitored daily and measured every 2–3 d. Tumor volume was determined as length (mm)×width^2 (mm)×0.5. C57BL/6 tumor-bearing mice were treated intraperitoneally with 500 µg αPD-1 monoclonal antibody (B16: clone 29 F.1A12; 3LL: clone J43, BioXCell) in 200 µL PBS on day 6, and 250 µg αPD-1 monoclonal antibody on days 8, 10, 12, 14 and 16 post tumor inoculation. Control mice received rat IgG (Jackson ImmunoResearch Laboratories, Inc.). For the B16-F10 studies, 1×10^5 tumor cells were intravenously injected into C57BL/6 mice. Mice were treated intraperitoneally with 500 µg α PD-1 monoclonal antibody (B16: clone 29 F.1A12) in 200 µL PBS on day −1, and 250 µg αPD-1 monoclonal antibody on days 1, 3, 5, 7 and 9 post tumor inoculation (d.p.i.). *ob/ob* mice were subcutaneously injected with 1×10^6 B16-F0 in 100 µL PBS in the right flank. 1 µg/g recombinant mouse leptin (rmleptin, R&D Systems, Minneapolis, MN) was injected intraperitoneally twice per day from d.p.i. −3 to 14.

Adoptive transfer of cells into mice. 2×10^7 cells from either C57BL/6 WT or BSK *db/db* mice isolated from spleens and lymph nodes were adoptively transferred into NSG mice. Immune parameters of B6 WT or BSK *db/db* T cells in the recipient of NSG mice were analyzed on day 13 post-transfer. 1×10^6 B16-F0 cells were subcutaneously inoculated in the right flank of 5–month-old male DIO and control Rag2$^{-/-}$ mice. The MagniSort Mouse T-cell Enrichment Kit (ThermoFisher) was used to enrich T cells from spleens and lymph nodes of B6 WT or BSK *db/db* mice. 2×10^6 enriched T cells from either B6 WT or *db/db* mice were adoptively transferred into B16-F0-bearing control and DIO Rag2$^{-/-}$ mice at 6 d.p.i. Immune parameters of B6 WT or *db/db* T cells in the recipient of B16-F0-bearing control and DIO Rag2$^{-/-}$ mice were analyzed on day 16 post-transfer.

Anti-CD40/IL-2 immunotherapy. The agonistic anti-mouse CD40 antibody (α CD40, clone FGK115B3) was generated via ascites production in our laboratory and 6- to 8-month-old male DIO and control B16-F0-bearing mice were treated with αCD40 and recombinant human IL-2 (rhIL-2, TECIN Teceleukin) as previously described[40,50]. In brief, αCD40 (40 µg/dose in 200 µL PBS) was administered daily for a total of 5 consecutive days (d.p.i. 6–10) and rhIL-2 (10^5 IU/dose) was administered twice on d.p.i. 7 and 9. B16F0-bearing mice treated with either αCD40/rhIL-2 or anti-PD-1 were bled on day 8. Control mice received rat IgG (Jackson ImmunoResearch Laboratories, Inc.) and PBS.

Mouse flow cytometry. Single cell suspensions were prepared from livers, tumors, spleens, lung and draining lymph nodes. Cells were incubated with Fc block (anti-CD16/32 clone 93, BioLegend) and stained with the fluorochrome-conjugated monoclonal antibodies listed below. FMOs were used as negative staining controls to set gates. For Intracellular staining of TNFα and IFNγ, the Cytofix/CytopermTM kit (BD Biosciences) was used. 1×10^6 single cells from spleen, liver, and tumors were stimulated with 1 µg/mL anti-mouse CD3 antibody coated wells (clone 145-2C11) in RF10 Complete Medium for 6 h total at 37 °C with 4 µL/6 mL GolgiStop (BD Biosciences) and 1 µL/mL GolgiPlug (BD Biosciences) for the last 4 h before surface staining. For intracellular staining of Ki67, FoxP3, T-bet and Eomes, the FoxP3/Transcription Factor Staining kit (ThermoFisher) was used. 2×10^5 cells from liver and spleen were stimulated with 1 µg/mL Concanavalin A (ConA, MilliporeSigma) for 48 h at 37 °C before surface staining. For pSTAT3 staining, $2–5\times10^5$ single cells from spleen were stimulated by 100 ng/ml anti-mouse CD3 antibody coated wells (clone 145–2C11) with or without 12 µM STAT3 inhibitor cryptotanshinone (EMD Millipore, CAS# 35825-57-1) for 1 h at 37 °C prior to addition of 100 ng/mL or 1000 ng/mL recombinant mouse leptin (rmleptin, Gibco LifeTechnologies). Intracellular pSTAT3 was stained based on the manufacturer's two-step protocol for fixation/methanol (IC Fixation Buffer, cat# 00-8222, ThermoFisher Scientific). Zombie Red viability dye and the following fluorochrome-conjugated monoclonal antibodies were purchased from BioLegend: PB-anti-CD45 (30-F11), PB-anti-CD44 (IM7), APC-Cy7-anti-CD45 (30-F11), BV711-anti-CD4 (RM4–5), BV785-anti-CD3 (17A2), BV605-anti-CD8a (53–6.7), PE-Cy7-anti-TNFα (MP6-XT22), Alexa Fluor 700-anti-Ki67 (16A8), Alexa Fluor 647-anti-T-bet (4B10); From ThermoFisher: FITC-anti-PD-1 (RMP1–30), FITC-anti-FoxP3 (FJK-16s), PE-eFluor 610-anti-Eomes (Dan11mag), PE-anti-Tim3 (RMT3–23), PerCP-eFluor 710-anti-Lag3 (eBioC9B7W), PE-anti-PD-L1 (MIH5), PE-Cy7-anti-CD62L (MEL-14), APC-anti-pSTAT3 (Tyr705) (LUVNKLA); and from BD Biosciences: APC-Cy7-anti-IFNγ (XMG1.2). Details of antibodies including dilutions used and validation can be found in Supplementary Table 3. Flow cytometry data were acquired on an LSR Fortessa flow cytometer (BD Biosciences) and analyzed using FlowJo software (Tree Star).

Mouse tumor staining. For histological staining, B16-F0 tumors from DIO or lean control mice were fixed in 10% paraformaldehyde and embedded in paraffin. Multiple 4 µm sections were cut for Hematoxylin and eosin (H&E) staining Slides were prepared and stained at Histology Consultation Services, Inc. (Everson, WA). H&E slides of tumor samples were reviewed by a dermatologist/pathologist (R. R. Isseroff). Images were captured by a BZ-9000 BioRevo Fluorescence Microscope equipped with 10× numerical aperture objective lens (KEYENCE, Canada).

Mouse lung whole-mount preparation. Lungs from B16-F10-bearing mice were collected, separated into five lobes and fixed in 10% neutral buffered formalin. Lung tissue was transferred to 70% alcohol for 2 h then to 100% alcohol for another 2 h. Lungs were then dehydrated using three changes of xylene (30 min, 1 h, 1 h), followed by processing through a graded series of alcohol. After rinsing in running tap water for 30 min, the tissues were stained with hematoxylin for 2 min. Lungs were destained in a 1% HCl solution for 15 min, then placed under running tap water for 30 min, 70% alcohol for 1 h, 100% alcohol for 1 h, and finally xylene for 1 h. Whole mounts were then submerged in methyl salicylate for storage.

^{18}F-FDG-PET scanning image analysis. Six-month-old control and DIO mice bearing B16-F0 tumors were analyzed for uptake of FDG by PET-CT image. Mice were anesthetized using vaporized isoflurane and oxygen. The radiotracer ^{18}F-FDG (7.92 ± 0.45 MBq) was administered via lateral tail vein injection. At 30 min post radiotracer injection, mice were placed in a prone position on the animal bed of a small-animal PET imaging system (Inveon DPET, Siemens Preclinical Solutions), and scanned. PET list mode data were acquired for 30 min. PET images were reconstructed using the 3D MAP reconstruction with a single hyperbolic prior (SP-MAP) provided by the vendor. After the PET scan, the animal bed was moved to an adjacent CT scanner (Inveon CT, Siemens Preclinical Solutions, Siemens Healthcare Molecular Imaging) for anatomical image acquisition. Animal respiration was visually monitored throughout both scans. Heat lamps were used to maintain consistent temperature. The PET and CT images were co-registered and analyzed using PMOD v3.8 software (PMOD Technologies). To determine tumor activity based on ^{18}F-FDG uptake in individual lesions, volumes of interest were drawn at sites of the tumors on overlay images, and the maximum standardized uptake value (SUV_{max}) was determined for each volume of interest.

MRI data acquisition and image analysis. Mice were anesthetized with isofluorane and oxygen. They were scanned on the Biospec 70/30 7.0 Tesla small-animal MRI system (Bruker Biospin Inc) using a 60 mm quadrature transmitter/receiver coil for whole body imaging. The scanning protocol consisted of the multi-slice with multi-echo (MSME) spin-echo sequence with a single echo and with respiratory gating to minimize breathing artifacts. Scan parameters were: TE 7.062, TR 775, conducted with and without chemical-selective fat suppression. Slice images were obtained in the coronal direction to improve spatial resolution while keeping scan time and TR at minimums. The in-plane matrix was 200×267 with a resolution of 0.3×0.3 mm. Forty-four slices were acquired with a slice thickness of 0.6 mm. Field of view was 6×8×2.64 cm. Difference images were generated by subtracting the fat-suppressed images from the non-fat-suppressed images, to identify the 3D distribution of fat deposits. Physiological monitoring (temperature and respiration) was used during the entire scan to ensure consistency and animal physiological stability.

RNA extraction, sequencing, analysis and PCR. Total RNA was extracted from sorted CD44+CD8+ T cells from spleen and lymph nodes using RNeasy plus mini kit (Qiagen). RNA concentrations were quantified using a Qubit fluorometer and RNA integrity was assessed using TapeStation 2200 (Agilent). Samples with an RNA integrity number ≥9 were used for this study. After QC procedures,

mRNA was submitted to Novogene for strand-specific library preparation and sequenced on a HiSeq 2500 instrument (150 pair-end sequencing). Data analysis was performed by the UC Davis Bioinformatics core using expHTS to trim low quality sequences and adapter contamination, and to remove PCR duplicates from raw reads. Trimmed reads for each sample were aligned to the GRCm38 mouse genome with GENCODE vM10 annotation, using STAR v. 2.5.2b aligner[51], which also generated raw counts per gene, which were the input to the statistical analysis. The Bioconductor package edgeR was used for read normalization[52]. The most significant pathways by functional interpretation of candidate gene lists were input and analyzed using G:Profiler by the g:GOST comprehensive method ($P < 0.05$). Network analysis was completed on up- and down-regulated genes in both CD4+ and CD8+ T cells from enriched gene sets using GeneMANIA[53].

RNA was extracted from tumor and liver tissue using a Qiagen RNeasy Lipid Tissue Mini kit (Qiagen, Valencia, CA) according to the manufacturer's protocol with optional on column DNase (Qiagen, Valencia, CA). RNA was quantified using Qubit 4 (ThermoFisher Scientific, Grand Island, NY) RNA Broad range and 300 ng RNA was converted to cDNA using Bio-Rad iScrpt Reverse Transcription Supermix (Bio-Rad, Hercules, CA) following standard protocols. qPCR was performed on a Bio-Rad CFX384 (Bio-Rad, Hercules, CA) with Bio-Rad SsoAdvanced Universal SYBR Green Supermix (Bio-Rad, Hercules, CA) in 10 µl using 5 ng cDNA. Primers for PD-1 (NM_008798.2): F-GCAGTTGAGCTGGCAATCAG, R-GGTGAAGGTGGCATTTGCTC; CPT1A (NM_013495.2): F-CACTGCAGCTCGCACATTAC, R-CCAGCACAAAGTTGCAGGAC; and HAVCR2 (NM_134250.2): F-CCTTGGATTTCCCCTGCCAA, R- CCCAGCACATAGGCACAAGT) were designed using Primer-BLAST on https://www.ncbi.nlm.nih.gov/tools/primer-blast/, and EOMES (Qiagen, PPM32970F-200) were compared to GAPDH (PPM02946E) (Qiagen, Valencia, CA) and β-actin (PPM02945B) (Qiagen, Valencia, CA) as reference genes.

Non-human primate studies. This study was performed at the California National Primate Research Center (CNPRC) under strict compliance with the NIH Guide for the Care and Use of Laboratory Animals. The CNPRC, which is one of seven centers supported by the National Institutes of Health, Office of the Director (NIH/OD), is accredited by AAALAC. The animal protocol was approved by UC Davis IACUC. Peripheral blood samples were obtained from adult (6- to 10-year old) male lean (7–9 kg) and obese (14.5–20 kg) rhesus macaques (*Macaca mulatta*). PBMCs were isolated by means of density centrifugation. Staining for flow cytometry was done using aqua viability dye (Invitrogen) and fluorochrome-conjugated antibodies against the following markers purchased from BioLegend: PE-anti-PD-1 (EH12.2H7) and BD Biosciences: PB-anti-CD3 (SP34-2), BV605-anti-CD4 (L200), AF700-anti-CD8 (RPA-T8), APC-anti-CD95 (DX2), and APC-H7-anti-CD28 (CD28.2)). Details of antibodies, including dilutions used and validation can be found in Supplementary Table 3. For the proliferation assay, 1×10^6 PBMCs were cultured for 4 d in an anti-CD3ε-coated 96-well round bottom plate (10 µg/mL, 50 µL/well 2 h incubation at 37 °C, followed by two washes with PBS), clone SP34, BD Biosciences). Cells were stained with the same surface marker antibody panel listed above and intracellular staining was performed with fixation/permeabilization solutions (BD Biosciences) to stain for Ki67 (clone B56 on AF488, BD Biosciences).

Human blood samples. Human blood collection study was approved by the IRB at the University of California at Davis. Human studies complied with all ethical regulations. Study participants were healthy female donors aged 27–56 years with no history of cancer, hypersensitivity, hyperglycemia and/or hyperinsulinemia. BMI for each participant was calculated as mass (kg)/height (m) ^2. Non-obese BMI was defined as <30 and obesity was defined as BMI ≥30. PBMCs were isolated from peripheral blood samples of each donor using Ficoll-Paque density centrifugation. Cells were stained with fluorochrome-conjugated monoclonal antibodies listed below in staining buffer with 1% human serum. Isotype-matched rat or mouse IgG monoclonal antibodies were used as negative staining controls Zombie Red viability dye and the following fluorochrome-conjugated monoclonal antibodies were purchased from BioLegend: BV605-anti-CD8a (RPA-T8), BV711-anti-CD4 (OKT4), PE-anti-PD-1 (EH12.2H7), AF700-anti-CD45RA (HI100); from BD: FITC-anti-CD62L (SK11), BV421-anti-CD3 (HIT3a), BV421-anti-CD45RO (UCHL1); and from ThermoFisher: APC-anti-Ki67 (20Raj1).

Naïve ($CD3^+CD45RA^+CD45RO^-$) versus effector/memory ($CD3^+CD45RA^-CD45RO^+$) T cells were isolated using a Beckman Coulter Astrios flow cytometric sorter. 2×10^5 cells were plated in each well and stimulated with 2.5 µg/mL ConA with or without the addition of 10 nM recombinant human leptin (rhleptin, Gibco LifeTechnologies) for 48 h at 37 °C in a 96-well flat-bottom plate. Cell were counted using an automated cell counter (Bio-Rad, TC20).

Human CD3 tissue staining. A serially collected cohort of patients with 152 colorectal cancer seen in the Yale Surgical Pathology suite was previously arranged into a tissue microarray (TMA) called YTMA 226 with annotated clinical data. This TMA was stained using validated and standardized multiplexed QIF panels as previously described[54]. We measured the levels of PD-1 (clone EH33, CST), CD3 (polyclonal, DAKO), and nuclear DAPI staining. Two TMA histospots were evaluated for each case and the average was obtained. Cases that have <5% tumor tissue in a histospot were excluded from the analysis. Quantitative measurement of the fluorescence signal was performed using the AQUA method of QIF. Differences in QIF between samples from non-obese (BMI < 30) and obese (BMI ≥ 30) patients were compared using a two-tailed Student's *t*-test.

TCGA analysis. TCGA-SKCM melanoma tumor mRNA expression data from 251 cases with clinical data including BMI were downloaded with the TCGAbiolinks[55] R package from the GDC legacy archive (https://portal.gdc.cancer.gov/legacy-archive/). Figures represent 126 patients (>60 years old). Differential expression analysis was carried out using the DESeq2[56] bioconductor R package (https://www.R-project.org/).

Human PD-(L)1 therapy clinical data. Using an IRB approved protocol, we reviewed all cancer patients, age 18 years or older, treated with anti PD-1 and PD-L1 therapy at the University of Oklahoma Health Sciences Center between January 2014 and January 2018 ($n = 250$). Simple descriptive statistics were created for all covariates (mean, SD for continuous covariates and n (%) for categorical variables) overall and by BMI group. Kaplan–Meier Analysis was performed to assess how BMI category (<30 versus ≥30) related to OS and PFS. A Cox proportional hazards model was used to assess the association of BMI category with OS and PFS adjusted for ECOG performance status, line of treatment, age, sex, and cancer type, checking for interactions between BMI category and other covariates[57].

Statistics. Graphs were made and statistical analyses were performed using Prism software (GraphPad Software Inc.). Data were expressed as mean ± s.e.m. For analysis of three or more groups, analysis of variance (ANOVA) tests were performed with a Bonferroni or Tukey post-hoc test, when appropriate. Analysis of differences between two normally distributed test groups was performed using the Student's *t*-test. *P* values were considered statistically significant if $P < 0.05$. Statistical outliers were identified using Grubb's test. Statistical differences in survival were determined by log rank (Mantel–Cox) analysis.

Data Availability

The datasets generated during and/or analyzed during the current study are available from the corresponding author on reasonable request. The datasets generated during and/or analyzed during the current study are available in the NCBI BioSample repository under accession numbers SAMN09873568 and SAMN09873569.

References

50. Mirsoian, A. et al. Adiposity induces lethal cytokine storm after systemic administration of stimulatory immunotherapy regimens in aged mice. *J. Exp. Med.* **211**, 2373–2383 (2014).
51. Bouchlaka, M. N. et al. Aging predisposes to acute inflammatory induced pathology after tumor immunotherapy. *J. Exp. Med.* **210**, 2223–2237 (2013).
52. Dobin, A. et al. STAR: ultrafast universal RNA-seq aligner. *Bioinformatics* 29, (15–21 (2013).
53. Robinson, M. D., McCarthy, D. J. & Smyth, G. K. edgeR: a Bioconductor package for differential expression analysis of digital gene expression data. *Bioinformatics* **26**, 139–140 (2010).
54. Warde-Farley, D. et al. The GeneMANIA prediction server: biological network integration for gene prioritization and predicting gene function. *Nucleic Acids Res.* **38**, W214–W220 (2010).
55. Villarroel-Espindola, F. et al. Spatially resolved and quantitative analysis of VISTA/PD-1H as a novel immunotherapy target in human non-small cell lung cancer. *Clin Cancer Res.* https://doi.org/10.1158/1078-0432.CCR-17-2542 (2017).
56. Cava, C. et al. SpidermiR: An R/Bioconductor package for integrative analysis with miRNA data. *Int. J. Mol. Sci.* https://doi.org/10.3390/ijms18020274 (2017).
57. Love, M. I., Huber, W. & Anders, S. Moderated estimation of fold change and dispersion for RNA-seq data with DESeq2. *Genome. Biol.* **15**, 550 (2014).

QUERY FORM

Nature Medicine	
Manuscript ID	**[Art. Id: 221]**
Author	**Ziming Wang**

AUTHOR:

The following queries have arisen during the editing of your manuscript. Please answer by making the requisite corrections directly in the e.proofing tool rather than marking them up on the PDF. This will ensure that your corrections are incorporated accurately and that your paper is published as quickly as possible.

Query No.	*Nature of Query*
Q1:	Please check your article carefully, coordinate with any co-authors and enter all final edits clearly in the eproof, remembering to save frequently. Once corrections are submitted, we cannot routinely make further changes to the article.
Q2:	Note that the eproof should be amended in only one browser window at any one time; otherwise changes will be overwritten.
Q3:	Author surnames have been highlighted. Please check these carefully and adjust if the first name or surname is marked up incorrectly. Note that changes here will affect indexing of your article in public repositories such as PubMed. Also, carefully check the spelling and numbering of all author names and affiliations, and the corresponding email address(es).
Q4:	Please note that after the paper has been formally accepted you can only provide amended Supplementary Information files for critical changes to the scientific content, not for style. You should clearly explain what changes have been made if you do resupply any such files.
Q5:	In Fig. 1h description, "PBMCs" correct as now defined: "peripheral blood mononuclear cells"?
Q6:	In sentence beginning with "Cpt1a was recently identified as being upregulated in early-stage…", LCMV correct as now spelled out: "lymphocytic choriomeningitis virus"?
Q7:	In fig 3j description, *** correct as now defined as "$P < 0.001$"?
Q8:	Please confirm that the edits to the sentence beginning "Importantly, tumor growth kinetics were similar regardless of…" preserve the originally intended meaning.
Q9:	Please provide brief definition for rIgG in Fig. 5a legend.
Q10:	In "Mice" section in Methods, please provide affiliation institution and city for Dr. R. Rivkah Isseroff and Dr. Jan Nolta in Methods.
Q11:	In RNA extraction, sequencing, analysis and PCR section in methods, in the first sentence of the second paragraph, please clarify what is meant by "optional on column DNase".
Q12:	Reference 57 was not originally cited in text. Please confirm that the citation of this reference after the sentence "…checking for interactions between BMI category…" is OK.
Q13:	Accession codes to not appear to be available from BioSample. Please confirm all codes will be released by online publication date and that codes and hyperlinks are correct.

QUERY FORM

Nature Medicine	
Manuscript ID	**[Art. Id: 221]**
Author	**Ziming Wang**

AUTHOR:

The following queries have arisen during the editing of your manuscript. Please answer by making the requisite corrections directly in the e.proofing tool rather than marking them up on the PDF. This will ensure that your corrections are incorporated accurately and that your paper is published as quickly as possible.

Query No.	*Nature of Query*
Q14:	Please provide the page range and volume number for reference 14.

nature research

Corresponding author(s): William J. Murphy

Reporting Summary

Nature Research wishes to improve the reproducibility of the work that we publish. This form provides structure for consistency and transparency in reporting. For further information on Nature Research policies, see Authors & Referees and the Editorial Policy Checklist.

Statistical parameters

When statistical analyses are reported, confirm that the following items are present in the relevant location (e.g. figure legend, table legend, main text, or Methods section).

n/a	Confirmed	
☐	☒	The exact sample size (*n*) for each experimental group/condition, given as a discrete number and unit of measurement
☐	☒	An indication of whether measurements were taken from distinct samples or whether the same sample was measured repeatedly
☐	☒	The statistical test(s) used AND whether they are one- or two-sided *Only common tests should be described solely by name; describe more complex techniques in the Methods section.*
☐	☒	A description of all covariates tested
☐	☒	A description of any assumptions or corrections, such as tests of normality and adjustment for multiple comparisons
☐	☒	A full description of the statistics including central tendency (e.g. means) or other basic estimates (e.g. regression coefficient) AND variation (e.g. standard deviation) or associated estimates of uncertainty (e.g. confidence intervals)
☐	☒	For null hypothesis testing, the test statistic (e.g. *F*, *t*, *r*) with confidence intervals, effect sizes, degrees of freedom and *P* value noted *Give P values as exact values whenever suitable.*
☒	☐	For Bayesian analysis, information on the choice of priors and Markov chain Monte Carlo settings
☒	☐	For hierarchical and complex designs, identification of the appropriate level for tests and full reporting of outcomes
☒	☐	Estimates of effect sizes (e.g. Cohen's *d*, Pearson's *r*), indicating how they were calculated
☐	☒	Clearly defined error bars *State explicitly what error bars represent (e.g. SD, SE, CI)*

Our web collection on statistics for biologists may be useful.

Software and code

Policy information about availability of computer code

Data collection	Bio-Rad CFX Maestro Software version 1.1, FlowJo V10, R version 3.4.0, Bioconductor package edgeR
Data analysis	Graphpad Prism V6.02, FlowJo V10, inForm, PMOD v3.8, STAR v. 2.5.2b, TCGAbiolinks v.2.6.12, DESeq2 bioconductor R package v.1.18.1

For manuscripts utilizing custom algorithms or software that are central to the research but not yet described in published literature, software must be made available to editors/reviewers upon request. We strongly encourage code deposition in a community repository (e.g. GitHub). See the Nature Research guidelines for submitting code & software for further information.

Data

Policy information about availability of data

All manuscripts must include a data availability statement. This statement should provide the following information, where applicable:

- Accession codes, unique identifiers, or web links for publicly available datasets
- A list of figures that have associated raw data
- A description of any restrictions on data availability

The datasets generated during and/or analyzed during the current study are available from the corresponding author on reasonable request. The datasets generated during and/or analyzed during the current study are available in the NCBI BioSample repository under accession # SAMN09873568, SAMN09873569, https://www.ncbi.nlm.nih.gov/biosample/9873568, https://www.ncbi.nlm.nih.gov/biosample/9873569.

Field-specific reporting

Please select the best fit for your research. If you are not sure, read the appropriate sections before making your selection.

☒ Life sciences ☐ Behavioural & social sciences ☐ Ecological, evolutionary & environmental sciences

For a reference copy of the document with all sections, see nature.com/authors/policies/ReportingSummary-flat.pdf

Life sciences study design

All studies must disclose on these points even when the disclosure is negative.

Sample size	Sample sizes were determined using standard power calculations using p=0.05 and power = 70% and estimating effect size from previous studies. Given the difficult to generate mouse models employed (i.e. DIO, NIA caloric restricted, DIO Rag2 -/-, etc.), in certain experiments the sample size was dictated by the availability of a limited resource. For human studies sample size was based on the number of patients or volunteers enrolled to previously designed studies.
Data exclusions	Outliers were identified using R package "extreamvalues", and when present, were winsorized from the analysis, so that the outliers were set equal to the nearest non-outlier value using pre-established criteria. For human blood assays analysis of statistical outliers was undertaken once the spread of the data was determined. Statistical outliers were identified and excluded using Grubbs test using pre-established criteria.
Replication	All experiments were succesafully replicated two to three times except where otherwise noted in the manuscript. Two experiments (adoptive transfer) were not replicated due to the limited quantities of difficult to generate mouse models. A single murine B16 tumor experiment which was performed with a different clone of anti-PD-L1 antibody was excluded. The general results of this experiment were similar to previously performed experiments (performed in duplicate) although this anti-body did appear to have some T cell depleting effects.
Randomization	In all experiments groups receiving therapy were randomly chosen. In tumor experiments groups were not created randomly but rather stratified based on size of implanted tumor to ensure that tumor sizes were roughly equivalent between groups prior to initiating any therapy.
Blinding	Blinding was not possible during data collection as obese mice can be easily distinguished from non-obese mice. Data analysis for mouse studies was independently assessed in a blinded manner by a second reviewer.

Reporting for specific materials, systems and methods

Materials & experimental systems

n/a	Involved in the study
☒	☐ Unique biological materials
☐	☒ Antibodies
☐	☒ Eukaryotic cell lines
☒	☐ Palaeontology
☐	☒ Animals and other organisms
☐	☒ Human research participants

Methods

n/a	Involved in the study
☒	☐ ChIP-seq
☐	☒ Flow cytometry
☒	☐ MRI-based neuroimaging

Antibodies

Antibodies used	Human: anti-PD-1 (clone EH33, CST), anti-CD3 (polyclonal, DAKO), BV421-anti-CD3 (HIT3a, BD), BV605-anti-CD8a (RPA-T8, BioLegend), BV711-anti-CD4 (OKT4, BioLegend); PE-anti-PD-1 (EH12.2H7, BioLegend); APC-anti-Ki67 (20Raj1, eBioscience). NHP:CD3 (SP34-2, PB, BD), CD4 (L200, BV605, BD), CD8 (RPA-T8, AF700, BD), CD95 (DX2, APC, BD), CD28 (CD28.2, APC-H7, BD), PD-1 (EH12.2H7, PE, BioLegend), Ki67 (B56, AF488, BD). Mouse:anti-CD3 (clone SP7, Abcam) and anti-PD1 (clone EPR20665, Abcam), Fc block (anti-CD16/32 clone 93, BioLegend),): PB-anti-CD45 (30-F11), PB-anti-CD44 (IM7), APC-Cy7-anti-CD45 (30-F11), BV711-anti-CD4 (RM4-5), BV785-anti-CD3 (17A2), BV605-anti-CD8a (53-6.7), PE-Cy7-anti-TNFα (MP6-XT22), FITC-anti-CD11c (N418), APC-Cy7-anti-I-A/I-E (M5/114.15.2), AF700-anti-Ki67 (16A8); From eBioscience (San Diego, CA): PE-anti-PD-L1 (MIH5), PE-Cy7-anti-PD-1 (RMP1-30), PE-Cy7-anti-CD62L (MEL-14).
Validation	Please see table at the end of this form for antibody catalog numbers, dilutions used, and references pertaining to antibody validation.

Eukaryotic cell lines

Policy information about cell lines

Cell line source(s)	4T-1, Lewis Lung Carcinoma (3LL), B16F0, and B16F10 were obtained from the ATCC
Authentication	Mouse cell lines were recently obtained from ATCC recently and not separately authenticated
Mycoplasma contamination	All cell lines tested negative for mycoplasma contamination
Commonly misidentified lines (See ICLAC register)	No commonly misidentified cell lines were used

Animals and other organisms

Policy information about studies involving animals; ARRIVE guidelines recommended for reporting animal research

Laboratory animals	Male and female C57BL/6NTac mice as well as male B6.129S6-Rag2tm1Fwa N12 (Rag2-/-) were purchased at 4 weeks age, generated into control or DIO mice and used between 6-12 months age as specified in the manuscript. B6.Cg-Lepob/J (ob/ob) mice and female B6.BKS(D)-Leprdb/J (B6 db/db) were used when they were 5-6 months old. 4-8 months old BKS.Cg-Dock7m +/+ Leprdb/J (BSK db/db) were used. 19 months old ad libitum (AL) and caloric restricted (CR) mice were obtained from the National Institute on Aging. For non-human primate studies blood was drawn from male Rhesus macaques (Macaca mulatta) from 6-10 years of age.
Wild animals	N/A
Field-collected samples	N/A

Human research participants

Policy information about studies involving human research participants

Population characteristics	For human healthy donor blood draws, blood was collected from 21 females mean age of 39 with age range of 27-60 and mean BMI of 30.4 and BMI range 18.8-50.6. In the human clinical study we analyzed data from 250 patients treated with PD-1/PD-L1 checkpoint inhibitors. For these patients mean BMI was 27.4, BMI range was 15-56.6, mean age was 61.7 and age range was 23-91, 45.6% were males. Fifty five patients had NSCLC, 45 had melanoma, 20 had ovarian, and 130 had other cancers. Seventy patients had ECOG performance status of 0, 134 had a performance status of 1, and 46 had a performance status of 2 or greater. Seventy patients had 1 prior line of therapy, 91 patients had 2 prior lines of therapy, and 115 patients had 3 or more prior lines of therapy.
Recruitment	For human healthy donor blood draws volunteers were recruited at the UC Davis Cancer Center. For the clinical study no specific recruitment strategy was employed as this was a retrospective analysis of patients previously treated with checkpoint inhibitors.

Flow Cytometry

Plots

Confirm that:

☒ The axis labels state the marker and fluorochrome used (e.g. CD4-FITC).

☒ The axis scales are clearly visible. Include numbers along axes only for bottom left plot of group (a 'group' is an analysis of identical markers).

☒ All plots are contour plots with outliers or pseudocolor plots.

☒ A numerical value for number of cells or percentage (with statistics) is provided.

Methodology

Sample preparation	Single cell suspensions were prepared from livers, salivary glands, tumors, spleens and draining lymph nodes using manual disassociation and DNAase / collagenase
Instrument	LSR Fortessa flow cytometer (BD)
Software	FlowJo V10
Cell population abundance	Post sort cell populations were generally >95% as determined by flow cytometry
Gating strategy	Gating was performed using fluorescence minus one groups to set the negative gate. Gating strategies are demonstrated in representative flow plots throughout the manuscript.

☒ Tick this box to confirm that a figure exemplifying the gating strategy is provided in the Supplementary Information.